

Investigating the flexural strength of recycled cast glass

Bristogianni, Telesilla; Oikonomopoulou, Faidra; Yu, Rong; Veer, Fred A.; Nijse, Rob

DOI

[10.1007/s40940-020-00138-2](https://doi.org/10.1007/s40940-020-00138-2)

Publication date

2020

Document Version

Final published version

Published in

Glass Structures and Engineering

Citation (APA)

Bristogianni, T., Oikonomopoulou, F., Yu, R., Veer, F. A., & Nijse, R. (2020). Investigating the flexural strength of recycled cast glass. *Glass Structures and Engineering*, 5(3), 445–487. <https://doi.org/10.1007/s40940-020-00138-2>

Important note

To cite this publication, please use the final published version (if applicable). Please check the document version above.

Copyright

Other than for strictly personal use, it is not permitted to download, forward or distribute the text or part of it, without the consent of the author(s) and/or copyright holder(s), unless the work is under an open content license such as Creative Commons.

Takedown policy

Please contact us and provide details if you believe this document breaches copyrights. We will remove access to the work immediately and investigate your claim.



Investigating the flexural strength of recycled cast glass

Telesilla Bristogianni · Faidra Oikonomopoulou ·
Rong Yu · Fred A. Veer · Rob Nijse

Received: 26 April 2020 / Accepted: 9 September 2020 / Published online: 2 November 2020
© The Author(s) 2020

Abstract Currently, tons of high quality commercial glass are down-cycled or landfilled due to contaminants that prevent close-loop recycling. Yet, this glass is potentially a valuable resource for casting robust and aesthetically unique building components. Exploring the potential of this idea, different types of non-recyclable silicate glasses are kiln-cast into $30 \times 30 \times 240$ mm beams, at relatively low temperatures (820–1120 °C). The defects occurring in the glass specimens due to cullet contamination and the high viscosity of the glass melt, are documented and correlated to the casting parameters. Then, the kiln-cast specimens and industrially manufactured reference beams are tested in four-point bending, obtaining a flexural strength range of 9–72 MPa. The results are analysed according to the role of the chemical composition, level of contamination and followed casting parameters, in determining the flexural strength, the Young's modulus and the prevailing strength-limiting flaw. Chemical compositions of favourable performance are highlighted, so as critical flaws responsible for a dramatic decrease in strength, up to 75%. The defects situated in the glass bulk, however, are tolerated by the glass network and have minor impact on flexural strength and

Young's modulus. The prerequisites for good quality recycled cast glass building components are identified and an outline for future research is provided.

Keywords Cast glass · Glass flexural strength · Glass defects · Recycling of glass waste · Mechanical properties of glass

1 Introduction

The great potential of glass casting technology for the building industry is so far little explored by structural engineers and architects, but are gradually getting discovered after the success of all cast-glass load bearing structures such as the Crystal Houses façade in Amsterdam (Oikonomopoulou et al. 2018c). The 3D-shaping possibilities provided by casting can offer robust glass components of larger cross-sections and a wider variety of forms and colours than currently available by other glass processing methods. Parallel to the recognition of the structural and aesthetical strengths of cast glass components, questions arise regarding their environmental impact and life-cycle. The use of currently not recyclable-disposed glass as a raw source for glass casting at lower temperatures, is a promising idea that addresses both the pressing problem of glass waste, and the urgency to lower the carbon footprint of glass building components (Bristogianni et al. 2018; Oikonomopoulou et al. 2018b). To specify the term “currently not recyclable glass”, apart from the suc-

T. Bristogianni (✉) · R. Yu · R. Nijse
Faculty of Civil Engineering and Geosciences, TU Delft,
Delft, The Netherlands
e-mail: t.bristogianni@tudelft.nl

F. Oikonomopoulou · F. A. Veer
Faculty of Architecture and the Built Environment, TU Delft,
Delft, The Netherlands

cessful recycling of soda lime glass food and beverage containers, the rest of the discarded—often high quality—commercial glass rarely meets the strict standards of the manufacturers due to contamination from coatings and/or adhesives. The lack of infrastructure for collection, product disassembly and cullet separation concerning these different types of glass, originates from the hesitation of the manufacturers to accept this cullet, and thus limits or prevents its recycling. Therefore, as this glass cannot flow back into the original product system (close-loop recycling), it gets down-cycled to applications such as aggregate, ceramic-based products, foam insulation, abrasives (Silva et al. 2017), or is disposed of in landfills. As the need of finding alternative routes, markets and end-users for the upcycling of the tons of high-quality discarded glass is imperative, the partial diversion of this waste into the building industry by casting structural glass components is worth exploring.

The above developments reveal a gap in the literature concerning the mechanical properties of cast glass components and the suggestion of a design strength for their structural use. This is linked with the absence of established manufacturing procedures and quality control standards, and thus the great variability in the strength of the cast glass products according to each manufacturer and the corresponding glass composition and casting process applied. The use of waste glass cullet is an added complication to this issue, giving rise to a series of traditional and new types of defects (Bartuška

2008; Bristogianni et al. 2019), which may compromise the strength of the glass product.

This paper explores the flexural strength of recycled cast glass—a property relevant to the engineering practice. Aim is to give insight into the effect of the casting parameters on the strength, and to assess the plausibility of employing waste glass for the production of safe structural components. Thus, in this work, a variety of commercial glass waste silicates is tested and evaluated for their ability to be kiln-cast into structural components at relatively low temperatures (820–1120 °C). The occurring defects are documented and correlated with the stage of production during which they are caused. Thereafter, two series of four-point bending experiments are conducted in kiln-cast glass beams of 30 × 30 × 240 mm dimensions. The results are analysed according to the role of the chemical composition, level of contamination and followed casting parameters, in determining the flexural strength and the origin of fracture. The testing of a limited number of industrially manufactured components serves as a point of reference.

2 Experimental work

2.1 Glass cullet categorization and specimen preparation

This work studies a series of characteristic commercial glasses, used for the production of common glass prod-

Table 1 Specimen preparation, cullet categorization and kiln-casting settings





















Glass type	Specimen description	Source	Composition* (main compounds in wt%)	Cullet contamination**	Cullet size (mm)	Cullet organisation in mould	Forming temperature in °C (10hr dwell)	Annealing temperature in °C (10hr dwell)***
	Fully Tempered float	IFS-SGT		Clean	shards =30*30*10		1120	560
	Fully Tempered float, fused	IFS-SGT		Clean	shards =30*30*10	Same as above	970	560
Soda Lime Silica (Float Glass)	Float 10mm, 3 horizontal layers, fused	IFS-SGT	75.4% SiO ₂ , 12.4% Na ₂ O, 7.6% CaO, 4% MgO, 0.4% Al ₂ O ₃	Clean	10*30*240		970	560
	Float 10mm, 24 vertical layers, fused	IFS-SGT		Clean	10*30*30		970	560
	Float 10mm, 3 vertical layers, fused	IFS-SGT		Clean	10*30*240		970	560
	Float dark blue	AGC	73.1% SiO ₂ , 12.8% Na ₂ O, 8.1% CaO, 4% MgO, 0.9% Al ₂ O ₃ , 0.76% Fe ₂ O ₃	Clean	shards thickness =3-4, width =3-20		1120	560

Table 1 continued

Glass type	Specimen description	Source	Composition* (main compounds in wt%)	Cullet contamination**	Cullet size (mm)	Cullet organisation in mould	Forming temperature in °C (10hr dwell)	Annealing temperature in °C (10hr dwell)***
	Float combo	Maltha Recycling	Variation of float glass recipes (Tested samples: 71.7-72.8% SiO ₂ , 12.2-12.5% Na ₂ O, 8.7-9.3% CaO, 3.5-3.8% MgO, 0.6-2% Fe ₂ O ₃ , 0.6-0.9% Al ₂ O ₃)	i) Coatings, ii) Float glass from various manufacturers, tints, iii. b,d) glass ceramics, different glass types	shards thickness =6, width =20-50		1120	560
Soda Lime Silica (Float Glass) with contamination	Oven doors	Coolrec	Variation of float glass recipes	i) Ceramic frit, ii) Float glass from various manufacturers, iii.a) Plastic	shards thickness =3-4, width =3-20		1120	560
	Car windshields	Maltha Recycling	Variation of float glass recipes	i) Coatings, ii) Float glass from various manufacturers, iii. a,b) traces of cardboard, sand, dust, PVB foil	coarse cullet =1-5		1120	560
	Float with black enamel, 60 vertical layers	AGC	Standard float glass recipe	i) Black enamel	4*30*30		1120	560
Modified Soda Lime	Poesia standard cast brick	Poesia	72.1% SiO ₂ , 15.9% Na ₂ O, 2.5% B ₂ O ₃ , 6.1% CaO, 1.9% K ₂ O, 0.9% Sb ₂ O ₃	Clean	chunks =50-100		1070	540
Borosilicate	DURAN tubes	Schott		Clean	curved shards, thickness =6-8, width =20-70		1120	560
	DURAN rods*10 vertical, 1.120°C	Schott		Clean	radius= 24, height= 50		1120	560
	DURAN rods*10 vertical, 1.070°C	Schott		Clean	radius= 24, height= 50	Same as above	1070	560
	DURAN rods*10 vertical, fused 970°C	Schott	80% SiO ₂ , 13% B ₂ O ₃ , 3.5% Na ₂ O, 2.7% Al ₂ O ₃ , 0.5% K ₂ O	Clean	radius= 24, height= 50	Same as above	970	560
	DURAN rods*2 vertical, fused 970°C	Schott		Clean	radius= 24, length= 240		970	560
	DURAN 24mm rods, honeycomb, fused 970°C	Schott		Clean	radius= 24, width= 30		970	560
	Borosilicate mix	Coolrec	Variation of borosilicate glass recipes, manually sorted	ii) Float glass from various manufacturers, iii. a,c) traces of plastic, cork, metal	thin shards, thickness ≤1, width =3-10		1120	560
Borosilicate mix	Maltha Recycling	Variation of borosilicate glass recipes, mechanically sorted	ii) Float glass from various manufacturers, iii. a,b,c,d) traces of plastic, cork, sand, dust, metal, different glass types	curved shards, thickness =1-4, width =5-30		1120	560	
Wertheim glass (C-glass)	Wertheim pellets	Glasmuseum Wertheim	63.8% SiO ₂ , 5.5% B ₂ O ₃ , 11.8% Na ₂ O, 6.4% CaO, 5.2% Al ₂ O ₃ , 3.7% MgO, 3.2% K ₂ O	Clean	=15*10*8		820	540
	Wertheim pellets	Glasmuseum Wertheim		Clean	=15*10*8	Same as above	900	540
Barium-Strontium silicate	Barium CRT front panel	From Philips CRT monitor	61.5% SiO ₂ , 8.1% SrO, 8% BaO, 7.2% Na ₂ O, 6.8% K ₂ O, 3.6% ZrO ₂ , 2.3% Al ₂ O ₃ , 1.1% CaO	Clean	shards, thickness =10, length 50-100		870	430
Potash-Lead silicate	Lead CRT funnel	Coolrec	Characteristic composition: 52% SiO ₂ , 22% PbO, 7.8% K ₂ O, 6.8% Na ₂ O, 4% Al ₂ O ₃ , 3.8% CaO, 1.8% MgO, 1% BaO	ii) Glass from different manufacturers	=5-15		870	430
	Lead glass	Royal Leerdam	57.7% SiO ₂ , 28.7% PbO, 9% K ₂ O, 3% Na ₂ O, 0.8% Sb ₂ O ₃ , 0.6% ZnO	i) Surface colour	shards, thickness =5-10, length 50-100		820	430

*All composition data derived by XRF measurements conducted with a Panalytical Axios Max WD-XRF spectrometer by Ruud Hendriks (TU Delft, 3me), apart from the SiO₂/B₂O₃ ratio in DURAN Schott derived from Heimerl (1999), the SiO₂/B₂O₃ ratio in Wertheim c-glass adjusted from Campbell (1975), the SiO₂/B₂O₃ ratio in Poesia glass derived from personal communication with the company and the characteristic CRT Funnel composition derived from Mueller (2012).

** The contamination source is organized as:

- i. Coatings (soft, hard, mirror, enamel, frit)
- ii. Variations in composition of the same glass type (different manufacturer, tints, colour)
- iii. External contaminants during sorting, namely: a. Organics (e.g. plastic, textiles), b. Non-glass inorganics (ceramics, stones, porcelain, glass ceramics), c. Metals, d. Different glass types

***All samples have been quenched to the annealing point with a rate of -160°C/hr

ucts such as float glass, glass fibers, cookware and laboratory glassware, cast glass bricks, crystal ware and CRT TV screens.¹ The choice of glasses is made in alignment with the types of waste glass cullet provided by various glass manufacturing and recycling companies, in order to address the recycling of readily available waste glass sources and thus tackle a realistic problem. X-ray fluorescent (XRF) analyses are conducted with a Panalytical Axios Max WDXRF spectrometer to define the chemical composition of the selected glasses. The provided cullet is thoroughly cleaned with isopropanol, and alien material (metal, plastic, cork) is manually removed when possible. The identified contaminants in the given cullet, still present in traces after the cleaning process, are listed in Table 1 according to the following categorization:

- i. Coatings (soft, hard, mirror, enamel, frit)
- ii. Variations in composition of the same glass type (different manufacturer, tints)
- iii. External contaminants during sorting: a. Organics (e.g. plastic, textiles), b. Non-glass inorganics (e.g. ceramics, stones, porcelain, glass ceramics), c. Metals, d. Different glass types (e.g. borosilicate, lead glass)

The cullet is then used for kiln-casting the $30 \times 30 \times 240$ mm glass beams required for the four-point bending tests. This particular beam size is selected as it provides a substantial thickness of cast material so that the influence of the defects in the bulk can be evaluated, while keeping the mass below 1 kg, and therefore reducing the annealing time. For each glass cullet, at least 3 samples are produced for statistical purposes.² The cullet is positioned inside of disposable silica/plaster investment moulds made from Crystalcast M248,³ in a structured or random manner. The moulds are then placed in a ROHDE ELS 200S or ELS 1000S electric



Fig. 1 Arrangement of the investment moulds inside the ROHDE ELS 1000S kiln

kiln (Fig. 1) and kiln-cast, meaning that only one kiln is employed for the complete casting process (heating up, forming, annealing and cooling).

The glass samples are formed at viscosities between 10^6 – $10^{3.5}$ dPa s and at top temperatures ranging from 820 to 1120 °C that are selected according to the chemical composition of each glass. The viscosity (η) range chosen is higher than the 10^4 – $10^{1.5}$ dPa s forming and melting range adopted by the glass industry, taking into account the risk of inhomogeneity of the final product. The approach of glass forming at lower temperatures is chosen on the one hand to reduce the required energy and corresponding CO₂ emissions, and on the other hand to intensify the occurrence of defects and evaluate if their existence is acceptable for a structural glass product. Thus for several samples (e.g. float glass, borosilicate rods), 2–3 different top temperatures are tested, corresponding to viscosity ranges of 10^{5-6} dPa s and 10^{3-4} dPa s, to further study the influence of the defects on the flexural strength. All specimens are kept at top temperature for 10 h,⁴ quenched at a -160 °C/h

¹ Cathode Ray Tube (CRT) screen production has ceased, yet there is still a considerable volume of CRT glass cullet resulting from the separation of disposed screens (Andreola et al. 2005).

² In case less samples are reported, the cullet available was not sufficient for the production of three samples. These specimens are nonetheless presented in this study to demonstrate the failure mode of the specific type of glass, rather than derive an absolute flexural strength value.

³ Crystalcast M248 is an investment powder consisting of 73% silica content (cristobalite, quartz), 23% calcium sulphate (gypsum) and 1% organics (Goodwin Refractory Services 2003; Gold Star 2019). The choice of the mould material is related to the kiln-casting technique followed in this work versus the commonly

Footnote 3 continued

reported casting by melt-quenching. As relatively low forming temperatures are chosen, the corresponding high viscosity of the heated glass does not allow its instant pouring from a melting (platinum or high-alumina) crucible to a preheated (steel or graphite) mould for annealing. Thus, the whole casting process has to take place in one mould that can withstand temperatures up to 1150 °C, does not attach to the glass and does not cause fracture to the specimen during cooling.

⁴ Given the high viscosity at top temperature and the size of the samples, a 10 h dwell is empirically found suitable for the removal of large bubbles (> 1 mm) and the incorporation of the coatings to the glass network.

rate down to their annealing point, heat-soaked for 10 h and cooled down to their strain point with a $-4\text{ }^{\circ}\text{C}/\text{h}$ ramp, before controllably cooled down to room temperature at a faster rate. This conservative annealing schedule guarantees stress-free specimens, as seen through cross-polarized light.

The specimens are produced at a 40 mm component height, and then cut to size with a water-cooled rotary diamond wheel cutter, to remove the top surface that often contains a high amount of flaws (e.g. surface crystallization, bubbles, depletion of alkali in the composition, wrinkling, crazing). Then, the specimens are ground and polished with a Provetro flat grinder and diamond abrasive discs in sequence of 60, 120, 200, 400 and 600⁵ grit and their resulting dimensions are documented. The inhomogeneities in the glass specimens are observed by naked eye and with the use of a Keyence VHX-5000 or VHX-7000 Digital Microscope. A qualitative assessment of the internal residual stresses in the glass specimens is achieved by using crossed-polarized filters. Lastly, the beams are prepared for the Digital Image Correlation (DIC) measurement by creating a speckle pattern on one of the longitudinal surfaces with elastic white and black spray paints.

The preparation process required for the production of the kiln-cast specimens is described in detail in Table 1. Apart from the kiln-cast specimens, the following industrially manufactured specimens are prepared and used as a reference:

- Beams cut out from standard Poesia⁶ cast glass bricks, ground and polished to a $30 \times 30 \times 240$ mm size
- Beams from 8/10 mm thick float glass plies, adhesively bonded with Delo Photobond 4468,⁷ ground and polished to a $30 \times 30 \times 240$ mm size

⁵ The 600 grit finishing is set according to ASTM C1161-13. In addition, Quinn et al. (2005) observe in their study on Machining Cracks in Ground Ceramics that sintered reaction bonded silicon nitride flexural specimens with 600 grit grinding fail due to material flaws rather than machining damage. This observation can be extended to glass specimens.

⁶ Poesia is the producer of the cast glass bricks for the Crystal Houses façade (Oikonomopoulou et al. 2018a).

⁷ This UV-curing acrylate is chosen because it forms a strong bond with the glass surfaces that leads to the monolithic behaviour of the glued sample (Oikonomopoulou et al. 2018a). Under four-point bending, the bonded glass sample is expected to show cohesive failure in the substrate (glass ply) and not delamination.

- Single 30×240 mm float glass panes of a 8/10 mm thickness, edges ground and polished

The grinding and polishing procedure followed for the preparation of the above specimens is identical to the one described for the kiln-cast samples. However, the bottom and top surface of the float glass specimens (single and bonded) is kept in its as received condition (optically fine polished) and only the cut edges are processed.

2.2 Four-point bending test set up

1st series of experiments (12 kiln-cast, 6 reference specimens)

The 1st series of experiments is conducted in order to provide a general overview regarding the flexural behavior of the different glass specimens. The specimens are tested using a Zwick Z10 displacement controlled universal testing machine in a laboratory air environment and at a rate of 0.2 mm/min. The four-point bending fixtures have a 110 mm span for the loading rollers and a 220 mm span for the support rollers, with 10 mm diameter fixed loading pins, and are loosely connected to the testing machine to allow some hinging (Fig. 2a).

2nd series of experiments (53 kiln-cast, 5 reference specimens)

The 2nd set of experiments involves the repeated testing of each glass category and provides accurate displacement data. The number of tested specimens per glass category is set to three, which is limited for testing a brittle material whose strength is by default statistical due to the randomness of the occurring flaws in the glass (Quinn et al. 2009). This study, however, aims to cover a broad variety of glass types and compare them according to their flexural behavior, in order to explore which recycled glass products have further potential for structural use. For these tests, a Schenck 100KN displacement controlled hydraulic universal testing machine is employed, and the specimens are tested in a laboratory air environment using a 0.3 mm/min displacement rate, which approximately corresponds to a 0.5 MPa/s rate.⁸ The four-point bending fixtures have a span of

⁸ A slightly faster displacement rate was chosen for the 2nd series, with the aim to reduce the total number of DIC images per experiment and thus confine the size of the files produced by the image processing software GOM Correlate to a maximum of

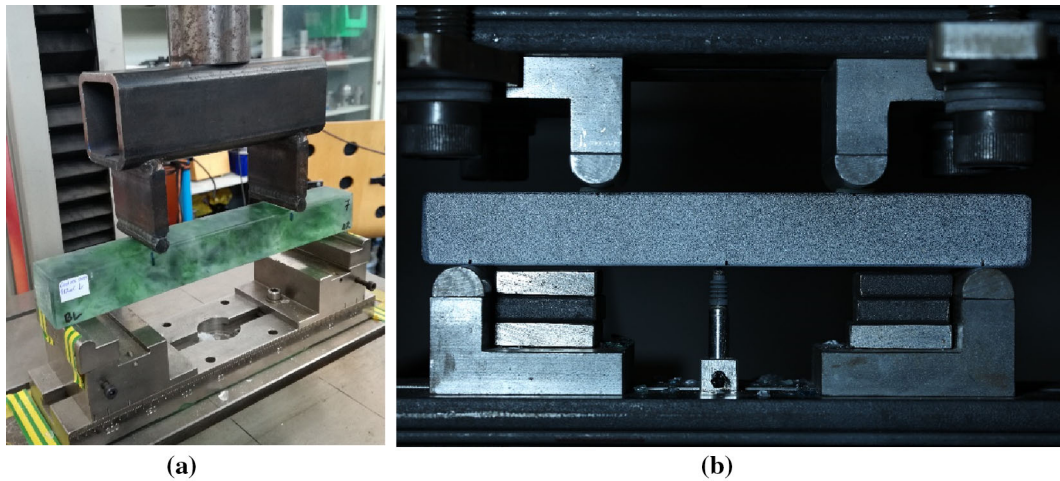


Fig. 2 **a** Fixtures and set-up of 1st series of four-point experiments. **b** Fixtures and set-up of 2nd series of four-point experiments. An LVDT sensor is placed at the middle of the span. The front surface of the specimen is covered with a speckle pattern

100 mm for the loading rollers and 200 mm for the support rollers, with 20 mm diameter fixed loading pins (Fig. 2b). To allow for minor adjustments and rotational movements, the support fixture is placed on a semi-circular pin, while the loading fixture is loosely connected to the testing machine. In addition, a 1 mm thick silicone rubber strip is placed between each loading pin and the specimen.

To measure the displacement of the beam due to bending, two methods are employed: 1) a Linear Variable Differential Transformer (LVDT) displacement sensor (Solartron AX 2.5 Spring Push Probe calibrated to a $0.5 \mu\text{m}$ accuracy) is placed under the middle point of the lower surface of the beam (measuring the point of maximum displacement), and 2) a 2D-DIC measurement, using a high-resolution (50.6MP) Canon EOS 5Ds camera that takes one picture per second of the speckled surface of the beam. The pictures of the 2D-DIC measurement are analysed using the GOM Correlate software. One image pixel corresponds to $31.5 \mu\text{m}$,

for the DIC measurement. The metallic strips placed next to the support pins are cushioning the specimen upon fracture and protect the LVDT sensor from damage. No contact occurs between the specimen and the strips during the bending test

therefore given the software accuracy of 0.05 pixel, any displacement above $1.57 \mu\text{m}$ can be captured.

Flexural strength and Young's modulus calculation

The flexural strength (σ) is computed from the equation below:

$$\sigma = \frac{3 \cdot F \cdot (L - L_i)}{2 \cdot b \cdot d^2} \quad (1)$$

where F the maximum load, L the support span, L_i the load span, b the beam's width and d the beam's height.⁹

The calculation of Young's (E) modulus is performed by correlating the force data obtained from the Schenck machine with (1) the maximum displacement from the LVDT sensor and (2) the maximum displacement from the DIC analysis (Fig. 3).

⁹ It should be noted that due to the fixed loading pins, a systematic positive error may occur due to a frictional constraint of $\mu \cdot F/2$ occurring at each pin, with μ being the coefficient of friction (Quinn et al. 2009). This force creates a counteracting moment of $\mu \cdot F \cdot d/2$, thus the above equation should be rewritten as:

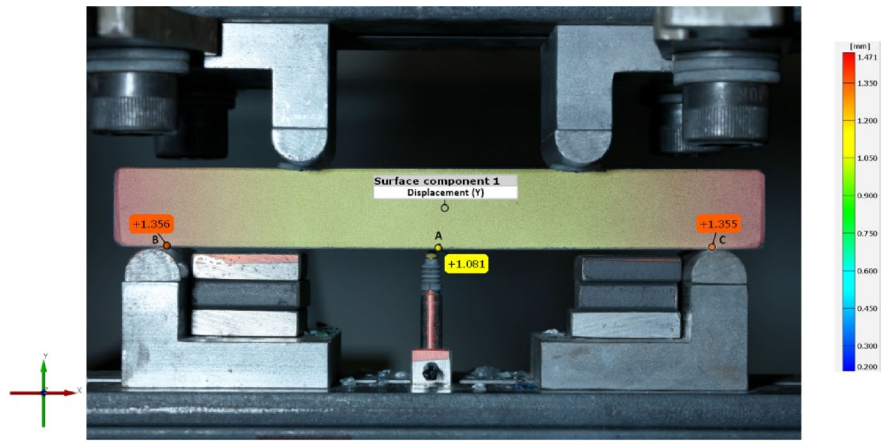
$$\sigma = \frac{3 \cdot F \cdot (L - L_i - \mu \cdot d)}{2 \cdot b \cdot d^2} \quad (2)$$

Assuming a moderate $\mu = 0,3$, the systematic error could be of magnitude 8.2% for the 1st series of experiments and 9% for the 2nd. However, due to insufficient data regarding the μ value, the flexural strength is not corrected in this study, and the reader should take into account the possibility of an error of approximately the aforementioned magnitude.

Footnote 8 continued

25 Gigabytes. Both the 1st and 2nd series displacement rates are below the rate of stress increase of $1.1 \pm 0.2 \text{ MPa/s}$ indicated by ASTM C158-02. A displacement controlled rate is favoured over force controlled, to avoid the crashing of the specimen upon failure, but also to allow for potential pop-ins (slight crack arrests) at maximum force, when the crack front interacts with an interface encountered in the glass mesostructure.

Fig. 3 Analysis of the displacement in y axis, using GOM Correlate software. The maximum displacement due to bending at point A is calculated by subtracting the total displacement at point A from the average displacement at point B and C



Given that the cross section of the beam in relation to the fixture spans results in a relatively stiff structural element, a shear deflection should be accounted to the total vertical deflection. The bending and shear deflection at mid-span with respect to the beam point above the support pins, and for a 1:2 four-point bending fixture ratio, are defined by the formulas below:

$$\Delta l_{Bending_mid} = \frac{11 \cdot \Delta F \cdot \left(\frac{L-L_i}{2}\right)^3}{12 \cdot E \cdot b \cdot d^3} \tag{3}$$

$$\Delta l_{shear_mid} = \frac{\Delta F \cdot \frac{L-L_i}{2}}{2 \cdot G \cdot b \cdot d} \tag{4}$$

where

$$G = \frac{E}{2 \cdot (1 + \nu)} \tag{5}$$

Adding the two segments of vertical deflection and solving towards the Young’s modulus, it is concluded:¹⁰

$$E = \frac{\Delta F}{\Delta l_{total_mid}} \cdot \left(\frac{11 \cdot \left(\frac{L-L_i}{2}\right)^3}{12 \cdot b \cdot d^3} + \frac{(L - L_i) \cdot (1 + \nu)}{2 \cdot b \cdot d} \right) \tag{6}$$

¹⁰ For the Young’s modulus calculation, the Poisson ratio of $\nu = 0.22$ of soda lime silica glass is used. Although among the tested glasses there may be a ± 0.02 deviation to this value, this has a negligible effect on the results.

3 Results

3.1 Defect evaluation for kiln-cast specimens

The flaws occurring in the surface and bulk of the produced glass specimens are qualitatively¹¹ documented according to type and cause. Aim is to correlate the defects found to the glass source used and followed casting and post-processing procedure, and to subsequently assess their contribution to the specimens’ flexural strength. The casting related defects are categorized¹² in:

1. Crystalline Inclusions
2. Glassy inhomogeneities (cord/ream)
3. Gaseous inhomogeneities (bubbles)

An overview of the defect categories and their causes is found in Fig. 4, based on which a documentation of the observed flaws per glass type is presented in Table 2.

¹¹ The quantitative analysis of the level of inhomogeneities in cast glass specimens of considerable cross section- and thus multiple layers of defects versus a thin-walled glass—is a complex process that involves several different testing methods (e.g. Computed Tomography Scanning to detect and measure density differentials, 3-dimensional Imaging Real-Time Polarimetry to define the location and shape of cord, etc). This analysis is kept out of the scope of this study as the main aim is to firstly identify the type and location of critical flaws that require future attention, and thus quantitative documentation.

¹² Categorization based on Bartuška (2008).

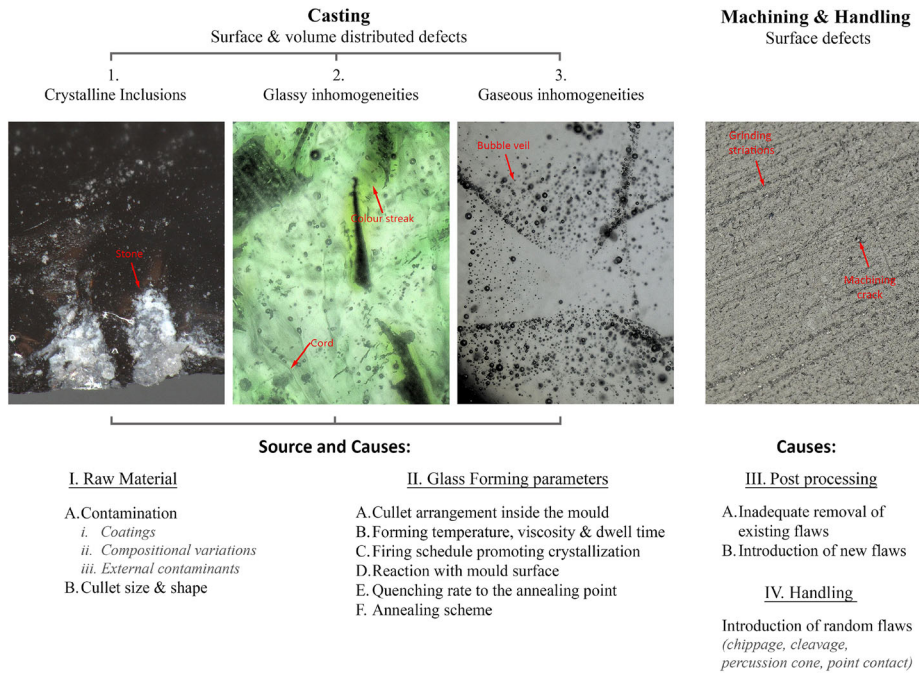



Fig. 4 Categorization and causes of the defects encountered in the kiln-cast glass specimens

Table 2 Evaluation of kiln-cast specimens

Glass type	Specimen description	Forming temperature in °C (10hr dwell)	Theoretical viscosity (log10(visc./poise)) at top temperature*	No. of successfully cast samples out of total castings	Type and cause of observed defects**	Kiln-cast specimen, side view
Soda Lime Silica (Float Glass)	Fully Tempered float	1120	3.5	9/9	1, 3 [II, B, D, III, A] Homogeneous glass of light aquamarine hue with evenly distributed miniscule bubbles. Occasional surface flaws from inadequate fusing of the cullet in combination with embedded material caused by contamination from the mould, challenging to be removed by post-processing.	
	Fully Tempered float, fused	970	5	1/1	1 [II, B, C, D, III, A] Crystallization along the fusion surfaces between the cullet pieces. Intense surface recessions in combination with embedded material caused by contamination from the mould due to inadequate fusing of the cullet at the exterior surfaces, challenging to be removed by post-processing.	
	Float 10mm, 3 horizontal layers, fused	970	5	3/3 (1 sample with surface creazing due to abrupt cooling)	1 [I, B, II, A, B, D] 2 horizontal layers of crystallization in the glass bulk.	
	Float 10mm, 24 vertical layers, fused	970	5	4/4 (1 sample with surface creazing due to abrupt cooling)	1 [I, B, II, A, B, D] 23 vertical layers of crystallization in the glass bulk, also exposed at the longitudinal surfaces of the beam.	
	Float 10mm, 3 vertical layers, fused	970	5	1/1	1 [I, B, II, A, B, D, E, III, A] 2 horizontal layers of crystallization in the glass bulk, also exposed at the top and bottom surfaces of the beam. Surface creazing due to reaction with the mould, challenging to be completely removed by post-processing.	
Soda Lime Silica (Float Glass) with contamination	Float dark blue	1120	3.5	3/3	3 [II, B] Homogeneous dark blue glass with miniscule bubbles	
	Float combo	1120	3.5	1/4	2, 3 [I, A, B, II, B] Heavily corded glass of light blue hue with colour streaks. 3/4 specimens fractured due to glass ceramic content in the cullet.	
	Oven doors	1120	3.5	4/4	1, 2, 3 [I, A, II, B, III, A] Colour streaks, flat crystalline inclusions (coating residue), occasional surface flaws from inadequate fusing of the cullet in combination with embedded material caused by contamination from the mould that are challenging to be removed by post-processing.	

Table 2 continued

Glass type	Specimen description	Forming temperature in °C (10hr dwell)	Theoretical viscosity (log10(Visc./poise) at top temperature*	No. of successfully cast samples out of total castings	Type and cause of observed defects**	Kiln-cast specimen, side view
Soda Lime Silica (Float Glass) with contamination	Car windshields	1120	3.5	3/3	1, 2, 3 [I, A, B, II, B, III, A] Colour streaks, bubbles, stones and flat crystalline inclusions (coating residue). Occasional surface flaws from inadequate fusing of the cullet in combination with embedded material caused by contamination from the mould, challenging to be removed by post-processing.	
	Float with black enamel, 60 vertical layers	1120	3.5	3/3	1 [I, A, II, A, B] Vertical layers of coating residue, also exposed at the longitudinal surfaces of the beam.	
Modified Soda Lime	Poesia standard cast brick	1070	3.5	3/3	3 [II, B] Transparent homogeneous glass with miniscule bubbles.	
Borosilicate	DURAN tubes	1120	4.5	6/6	3 [I, B, II, B] Dense veils of bubbles, along the connection surfaces of the glass shards.	
	DURAN rods*10 vertical, 1120°C	1120	4.5	5/5	3 [II, B] Transparent homogeneous glass with miniscule bubbles	
	DURAN rods*10 vertical, 1070°C	1070	5	3/3	3 [I, B, II, A, B] Transparent homogeneous glass with miniscule bubbles organized in vertical veils, also exposed at the longitudinal sides of the beam.	
	DURAN rods*10 vertical, fused 970°C	970	6	4/4	1, 3 [I, B, II, A, B, C] Vertical crystallized layers, also exposed at the longitudinal sides of the beam. Few bubbles in proximity to the fusion layers.	
	DURAN rods*2 vertical, fused 970°C	970	6	1/1	1, [I, B, II, A, B, C] One horizontal crystallized layer.	
	DURAN 24mm rods, honeycomb, fused 970°C	970	6	1/1	1, 3 [I, B, II, A, B, C] Crystallized layers in a honeycomb structure, also exposed at the longitudinal sides of the beam. Few bubbles in proximity to the fusion layers.	
Borosilicate mix	Coolrec	1120	4.5	1/1	1, 3 [I, A, II, B] Miniscule bubbles and occasional stones in the glass bulk.	
	Maltha	1120	4.5	0/3	1, 3 [I, A, II, D] Intense crystallization formed at the top surface, bubbles, heavy reaction with the mould that lead to fracture during cooling due to the different coefficient of thermal expansion of the two materials.	
	Wertheim pellets	820 / 900	6 / 5	3/3	1, 3 [II, B] Fusion lines and bubbles	
Barium-Strontium silicate	Barium CRT front panel	870	5.5	3/3	3 [II, B] Homogeneous dark black glass	
Potash-Lead silicate	Lead glass	870	-	1/1	1, 2, 3 [I, A, II, B] Heavily corded glass, bubbles, crystalline inclusions.	
	Lead glass	820	5.5	2/2	2, 3 [I, A, II, B] Colour streaks, bubbles.	

*Estimation based on the chemical composition, using the viscosity model by Fluegel (2007).

** The defects are categorized as: 1. Crystalline Inclusions, 2. Glassy inhomogeneities (cord/ream), 3. Gaseous inhomogeneities (bubbles)

The cause of these defects can be associated with the: I. Raw Material (A. Contamination, B. Cullet size and shape), II. Glass forming (A. Cullet arrangement in the mould, B. Forming temperature and corresponding viscosity in relation to dwell time, C. Firing schedule in combination with temperature differentials in the kiln that promote crystallization, D. Reaction with mould surface, E. Quenching rate to the annealing point, F. Annealing scheme), and III. Post processing (A. Inadequate removal of existing flaws).

In more detail, the cause of these defects is associated with one or more of the following manufacturing stages^{13, 14}:

I. Raw Material.

A. Contamination.

i. Coatings.

Several “flat” defects are observed in kiln-cast specimens from float glass cullet covered with enamel paint or ceramic frit, due to the insufficient melting of the coatings (Fig. 5). The XRF analyses of two characteristic coatings (Table 3) show compositions rich in high melting-point metal oxides and in particular in chromium(III) oxide (melting point of Cr_2O_3 is 2435 °C, NIH Database). The X-ray diffraction (XRD)¹⁵ analysis of kiln-cast glass samples (Fig. 6) shows in these cases the presence of eskolaite (mineral name of chromic oxide).

ii. Minor compositional variations.

Minor compositional variations lead to glassy inhomogeneities such as cord and colour streaks. Some examples with heavy striation are identified in the “Float combo” and “Lead CRT” (Fig. 7) samples.

iii. External contaminants.

In this category, the presence of glass ceramics or chemically different families of glass in the cullet (not detectable by eye, e.g. aluminosilicate shards in borosilicate or soda lime silica cullet), is the most critical, leading to specimens which fracture upon cooling, due to strains caused by thermal expansion variations. This is experienced in the “Float combo” (Fig. 8a) and

“Borosilicate mix Maltha” specimens.

More specifically, the “Float combo” specimens were cast by employing a compilation of flat glass shards (of approx. 20–50 mm width) provided by Maltha Recycling. This flat glass compilation is rejected from the recycling stream as the erroneous deposition of glass ceramic plates (e.g. cooktops) in the flat glass collection container—an often encountered phenomenon—renders the entire container unsuitable for recycling. The XRF and XRD analyses of characteristic pieces from the flat glass compilation sample (Table 4; Figs. 8b, 9) place the contaminants in the commercially applicable lithium aluminosilicate glass ceramics system, which is characterized by the close to zero thermal expansion coefficient (Höland and Beall 2020). The very low thermal expansion coefficient (CTE) contrasts with the typical $9.5 \times 10^{-6}/\text{K}$ (at 20–300 °C) of float glass (Shelby 2005), leading to unavoidable cracking. However, the reduction of the flat-glass compilation sample’s particle size (fine cullet or powder), could minimize the strains in the final cast product, and therefore this strategy requires further investigation.

Traces of metal, clay or stone lead to crystalline inclusions of a maximum of 2 mm size, but these are tolerated by the glass network (Figs. 10, 11). However further study is required to identify the crystalline inclusions (employing scanning electron microscopy) and to test if their role remains neutral when the glass is subjected to temperature gradients.

B. Cullet size and shape.

In the addressed glass viscosity range, the geometry of the cullet is often reflected in striations and/or three-dimensional bubble veils in the final glass component. In cases of very fine cullet (e.g. “Car Windshields” samples) this geometry is not distinguishable, and a rather high content miniscule bubbles prevails (Fig. 12).

¹³ In Table 2, flaws caused during stages III.B. and IV (post-processing and handling flaws) are not mentioned as they are not linked to the material and its casting method, but are rather arbitrary and only relevant to the fracture analysis of each specific specimen.

¹⁴ The following microscope images were made using a Keyence VHX-5000 or VHX-7000 Digital Microscope.

¹⁵ All XRD analyses in this work were conducted using a Bruker D8 Advance diffractometer, Bragg-Brentano geometry and Lynxeye position sensitive detector.

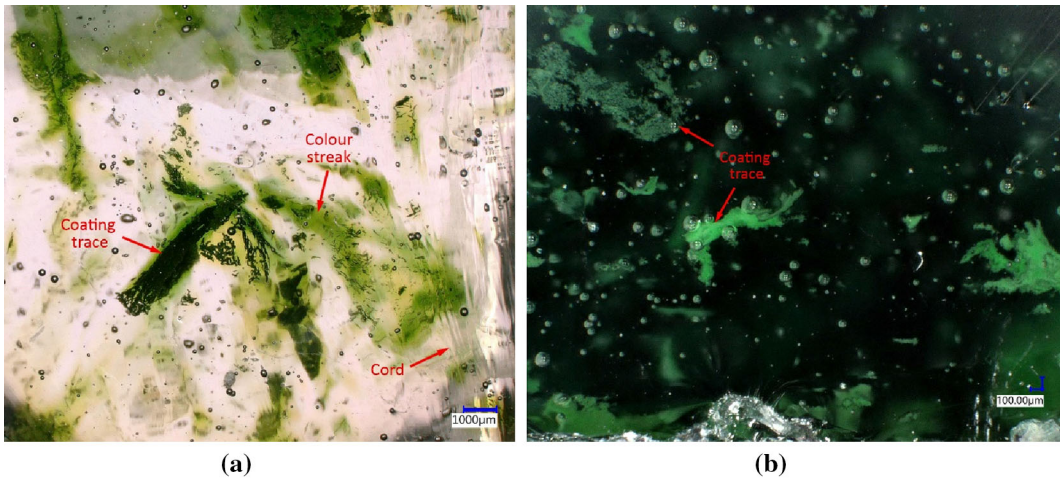


Fig. 5 **a** Microscope image of a “Oven doors, 1120 °C” kiln-cast glass with flat crystalline inclusions, cord, colour streak (due to partially molten coating material) and bubbles. **b** Microscope

image of a “Car windshields, 1120 °C” kiln-cast glass with crystalline inclusions and bubbles

Table 3 Coating composition

Coating type	Glass source	Composition ^a (wt%)										
		SiO ₂	Bi ₂ O ₃	C ₂ O ₃	CuO	PbO	Na ₂ O	TiO ₂	Fe ₂ O ₃	Al ₂ O ₃	CdO	ZnO
Black enamel	Enamel float, AGC	30.7	28.6	19.4	10.2		3.3	4.2				1.3
Black frit	Oven door, Coolrec	33.2		22.5	10.6	12.7	7.2	2.2	3.8	3.6	2.9	

^aXRF measurements conducted with a Panalytical Axios Max WD-XRF spectrometer by Ruud Hendrikx. The absolute wt% obtained by the XRF measurements may not be entirely accurate in the case of thin coatings, due to the extremely small thickness of the coating

Fig. 6 XRD pattern of kiln-cast “AGC Float with black enamel” glass at 1120 °C. The sample is at a large extent amorphous (black curve) yet it presents some sharp crystalline peaks (coloured sticks)

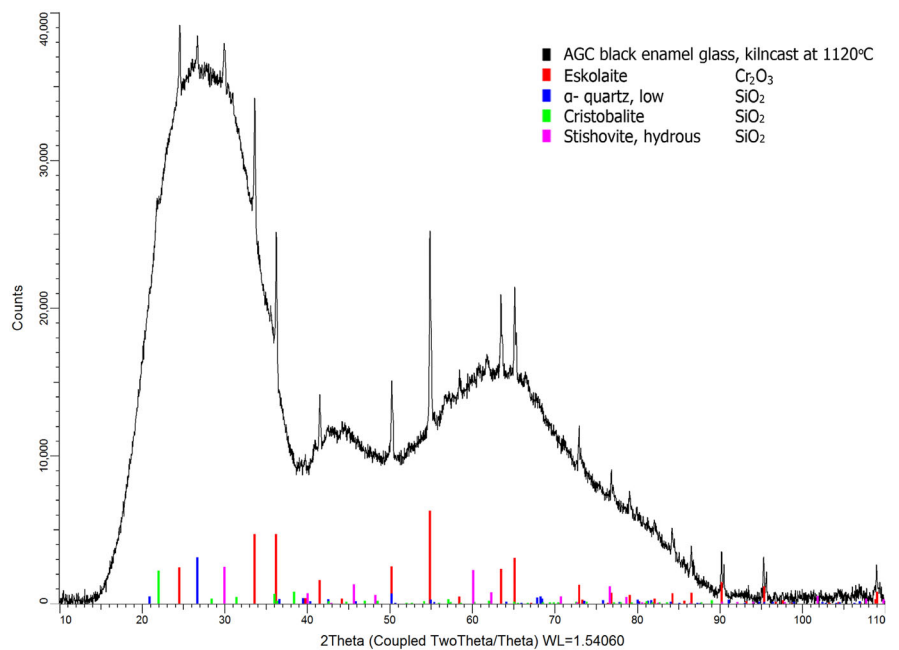


Fig. 7 “Lead CRT, 870 °C” specimen containing intense cord (seen as wavy lines) and bubbles

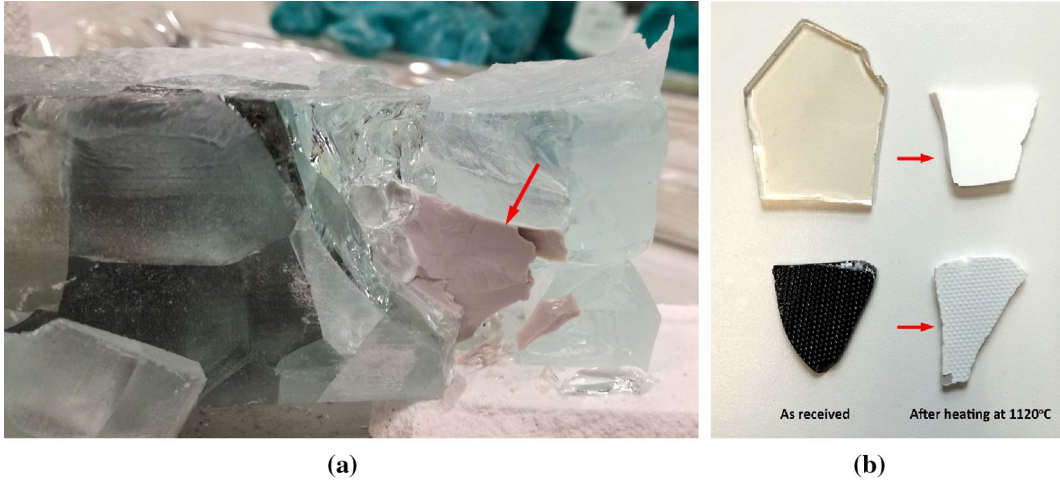


Fig. 8 a Fractured “Float combo, 1120 °C” specimen due to glass ceramic contamination. **b** Glass ceramic shards encountered in the flat glass compilation sample. The left column shows the shards in the “as-received” transparent condition, whereas the right column shows their opaque version after heat-treatment at

1120 °C for 10h. This behavior suggests a lithium aluminosilicate β -quartz solid solution phase in the transparent condition that transforms to β -spodumene during heat-treatment at temperatures above 1000 °C. The larger crystals in the later condition scatter the light and lead to opacity (Shelby 2005)

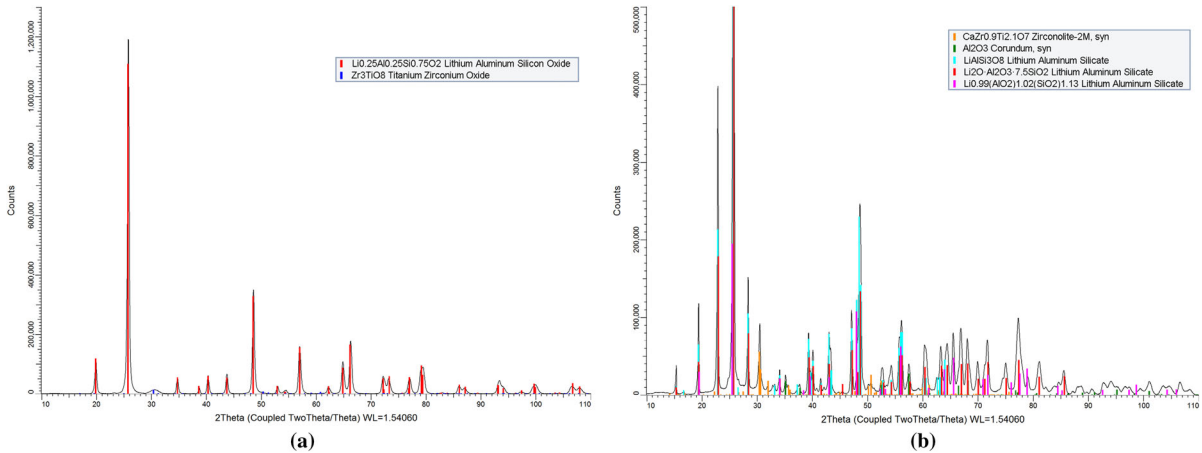


Fig. 9 XRD pattern of the yellow transparent glass ceramic depicted in Fig. 8b, in the as received condition (a) and after heat-treatment at 1120 °C for 10h (b). The crystal structure in b is similar to β -spodumene, yet the material presents multiple phases

Table 4 Chemical composition, crystal phase and CTE of typical lithium aluminosilicate glass ceramics, compared to the tested glass ceramic samples, the cast “Float Combo Maltha” specimen and a typical window glass

Type	Stage	Colour/transparency	Crystal		Coefficient of Thermal Expansion (20, 300°C): 10 ⁻⁷ /K	Composition* (wt%)																
			Type	Source		SiO ₂	Li ₂ O	Al ₂ O ₃	TiO ₂	ZrO ₂	ZnO	P ₂ O ₅	BaO	MgO	Na ₂ O	K ₂ O	As ₂ O ₃	Sb ₂ O ₃	V ₂ O ₅	Fe ₂ O ₃	CaO	Source
Piece selected from the “Float combo Maltha” sample (Fig. 8b)	As received	Light yellow transparent	Lithium Aluminum Silicon Oxide: Li _{0.22} Al _{2.35} Si _{0.76} O ₂	[1]	70.99*	*	20.98	2.06	2.05	0.01	1.37	1.26	-	0.52	0.22	0.4	0.08	-	0.02	0.02	[2]	
	After heating at 1120°C for 10hr	White opaque	Titanium Zirconium Oxide: Zr ₃ TiO ₆	[1]	Not verified																	
Piece selected from the “Float combo Maltha” sample (Fig. 8b)	As received	Dark brown transparent	Lithium Aluminum Silicate: LiAlSi ₃ O ₈ , Li ₂ O-Al ₂ O ₃ -7.5SiO ₂ , Li _{0.98} (AlO ₃) _{2.92} (SiO ₂) _{1.13}	[1]	70.62*	*	19.02	2.13	2.29	0.01	1.12	1.29	-	1.515	1.25	0.41	0.08	-	0.04	0.03	[2]	
	After heating at 1120°C for 10hr	Transparent with white opaque zones and brown colour streaks	Zirconolite-2M: Ca ₂ Fe ₃ Ti ₂ O ₇ , Corundum: Al ₂ O ₃	[1]	Not verified																	
“Float combo Maltha” cast sample (containing float glass and glass ceramic)	After heating at 1120°C for 10hr	Transparent with white opaque zones and brown colour streaks	Mainly amorphous with crystal phases: γ-Magnesium Silicate: Mg ₃ (SiO ₄), Quartz: SiO ₂ , Zirconium Oxide: ZrO ₂ , Cristobalite low: SiO ₂	[1]	Multiple CTE values	66.36	**	11.92	1.88	1.16	1.31	0.06	0.35	2.09	10.11	0.26	0.36	-	0.15	0.1	3.28	[2]
Schott Nextrema® 724-3	N/A	Light yellow transparent	Lithium Aluminosilicate	[3]	-0.28 [4]	50-80	0-5	15-27	0-5	0-5	0-5	-	0-8	0-8	0-2	0-2	-	-	-	-	0-8	[5]
Schott Nextrema® 712-3	N/A	Dark brown transparent	Lithium Aluminosilicate	[3]	-0.16 [4]																	
Schott Ceran®	N/A	Not verified	β-quartz solid solution	[3]	±0.15 [6]	64	3.5	21	2.3	1.6	1.5	-	2.5	0.1	0.6	0.5	-	0.85	-	0.23	0.2	[6]
Corning Vision®	N/A	Yellow transparent	β-quartz solid solution	[7]	Not verified	68.8	2.7	19.2	2.7	1.8	1	-	0.8	1.8	0.2	0.1	0.8	-	-	0.1	-	[7]
Corning USA018512A sample no. 2	N/A	Light lavender transparent	β-quartz solid solution	[8]	0.78 [8]	68.8	3	19.6	3	1.5	1.2	-	2.2	-	-	0.7	-	-	-	-	-	[8]
Corning 9617	N/A	White opaque	β-spodumene solid solution	[8]	3.2 [9]	67.4	3.5	20.4	4.8	-	1.2	-	1.6	0.2	0.1	0.4	-	-	-	-	-	[10]
Typical Soda Lime Silica window glass (float)	N/A	Clear transparent	Amorphous	-	9.5 [7]	73	-	0.1	-	-	-	-	-	4	14	-	-	-	-	0.1	9	[7]

*Lithium is a light element that cannot be detected by the XRF analysis and therefore the percentage corresponding to lithium oxide is reflected to a higher content of silica dioxide. According to the bibliography, the presented composition should have a 2-3% lithium oxide content and a lower silica dioxide content by 2-3%

**A lower than 3% lithium oxide content is expected in the chemical composition

[1] XRD measurements conducted by Ruud Hendriks (TU Delft, 3me) using a Bruker D8 Advance diffractometer, Bragg–Brentano geometry and Lynxeye position sensitive detector

[2] XRF measurements conducted with a Panalytical Axios Max WD-XRF spectrometer by Ruud Hendriks (TU Delft, 3me);

[3] Montazerian et al. (2015); [4] Songhan Plastic Technology Co., Ltd.; [5] Schott (2015b); [6] Höland and Beall (2020); [7] Shelby (2005); [8] Chyung (1977); [9] Brennan (1979); [10] Campbell and Hagy (1975)

Fig. 10 **a** Microscope image of “Lead CRT, 870 °C” specimen, containing undissolved blue particles of—most probably—cobalt oxide. **b** The variable inclusions in the “Borosilicate mix Coolrec, 1120 °C” specimen are tolerated by the glass network

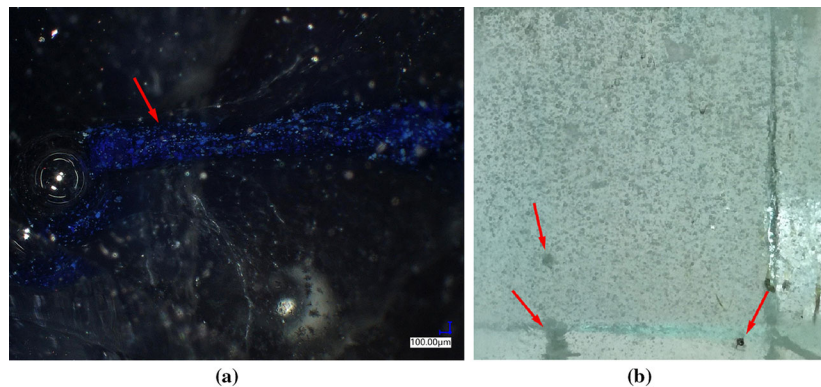


Fig. 11 Crystalline inclusions and bubbles detected in the bulk of a “Schott DURAN tubes 1120 °C” specimen, viewed through cross-polarized light. Although some inclusions e.g. the depicted 62.5 μm stone, induce stress to the surrounding glass, this is well tolerated within the 30 × 30 mm glass cross section

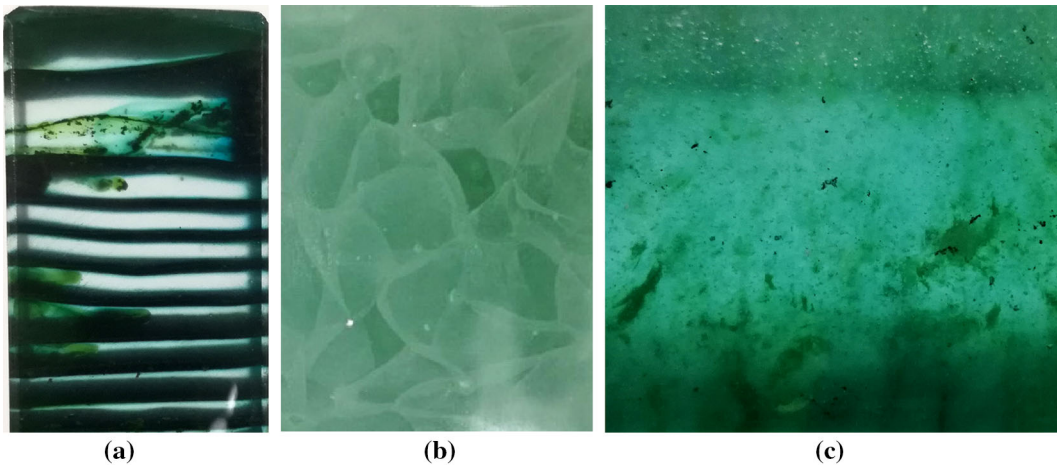
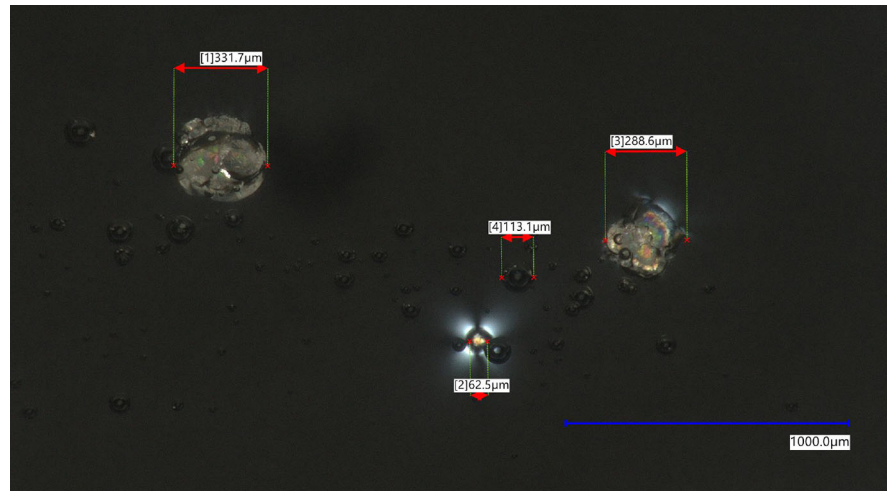


Fig. 12 The size, shape, and arrangement of the cullet, in combination with the forming temperature, lead to organized (a), random visible (b) and random non-traceable (c) meso-structures in the glass component. **a** “AGC float with black enamel, 1120 °C”

(image width ≈ 30 mm), **b** “Wertheim, 820 °C” (image height ≈ 30 mm), **c** “Car windshields, 1120 °C” (image height ≈ 30 mm)

II. Glass forming.

A. Cullet arrangement in the mould.

This is relevant with the geometry of the cullet (I. B) in combination with the firing schedule and corresponding viscosities of the formed glass (II. B, C). A defined cullet shape and high viscosity can lead to organized meso-structures composed of bubble veils (Figs. 13b, 14), cord or crystallized interfaces which result in a more predictable failure pattern (Fig. 13). Such organized structures also help in distinguishing the role of these defects when present at the glass surface or in the bulk.

B. Forming temperature and corresponding viscosity in relation to dwell time.

The top temperature affects the level of homogenization and the content of air-bubbles. All samples present minuscule bubbles due to the relatively low forming temperatures. In addition, the “cage” principle describing the mixing of dense liquids is applicable in this case, meaning that most of the molecules corresponding to an initial cullet piece will remain in the same position in relation to their neighboring cluster of molecules (cullet piece). The level of diffusion is increased when a viscosity of $10^{3.5}$ dPa s magnitude is reached, but it does not in any case

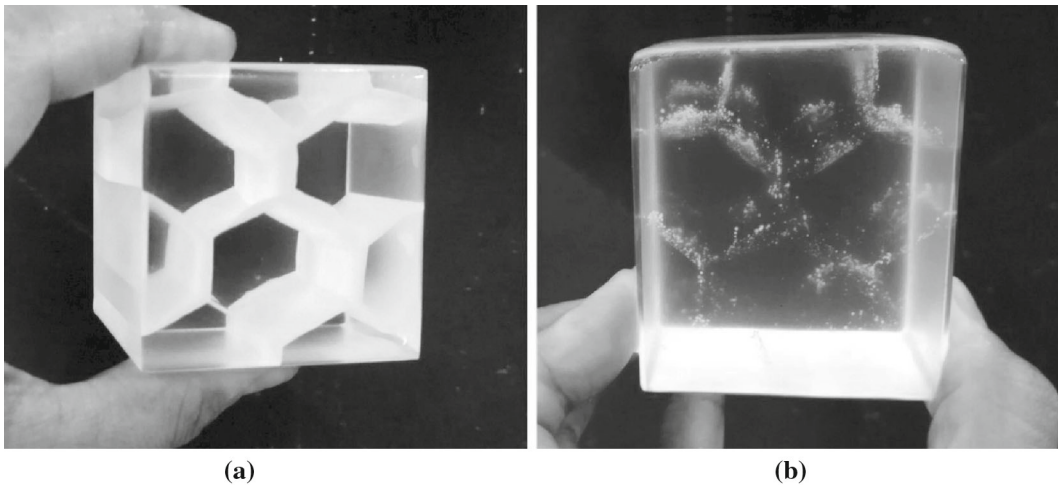
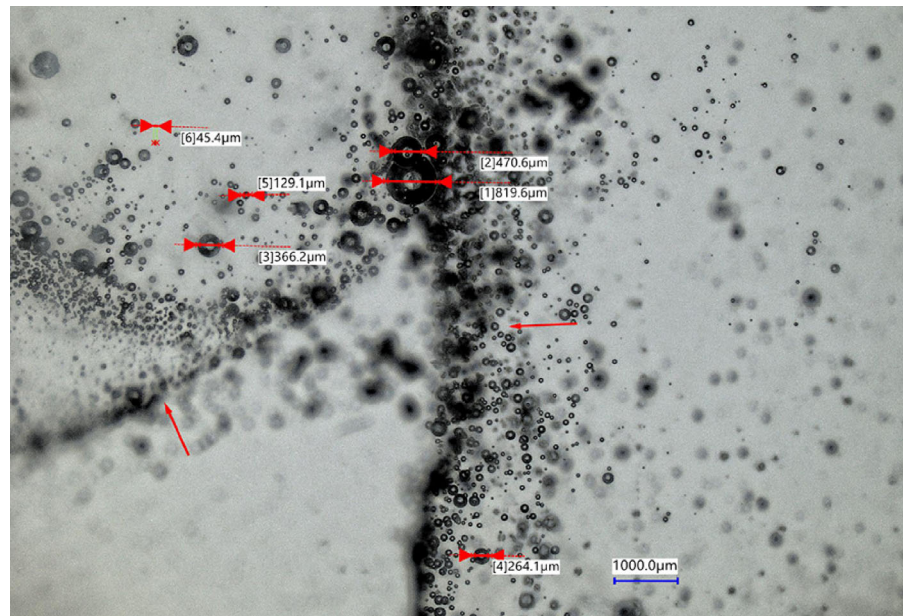


Fig. 13 Kiln-cast experiments with Schott DURAN borosilicate rods of 24 mm diameter forming 50 mm cubic samples. **a** Crystallized hexagon structure, engineered at 970 °C. **b** Bubble-veil hexagon structure engineered at 1120 °C

Fig. 14 Bubble veil observed in a “Schott DURAN tubes 1120 °C” specimen. The maximum bubble diameter is less than 1 mm, while the majority of the bubbles has a diameter below 0.2 mm



lead to a fully mixed glass in the given dwell time (see Figs. 12, 13).

- C. Firing schedule in combination with temperature differentials in the kiln that promote crystallization.

This is particularly applicable for the float and borosilicate glass samples formed at 970 °C. In these samples, the complete interface between each cullet piece is crystallized. According to the XRD analysis (Fig. 15), the borosilicate samples develop b-cristobalite crystals, while the float glass samples wollastonite 2M, b-

cristobalite and devitrite (Figs. 16, 17). Crystallization is favoured because the samples are formed below their liquidus point (T_L is around 1080 °C for the specific float glass, and around 1200 °C for the specific borosilicate¹⁶) yet reaching a low enough viscosity that kinetically allows nucleation. Nucleation starts at the interfaces, as there, a local compositional variation occurs due to the volatilization of alkali

¹⁶ The liquidus point of glasses T_L is found around a viscosity of 10^4 dPa s, and is estimated from the chemical composition of the given glasses according to Fluegel (2007a).

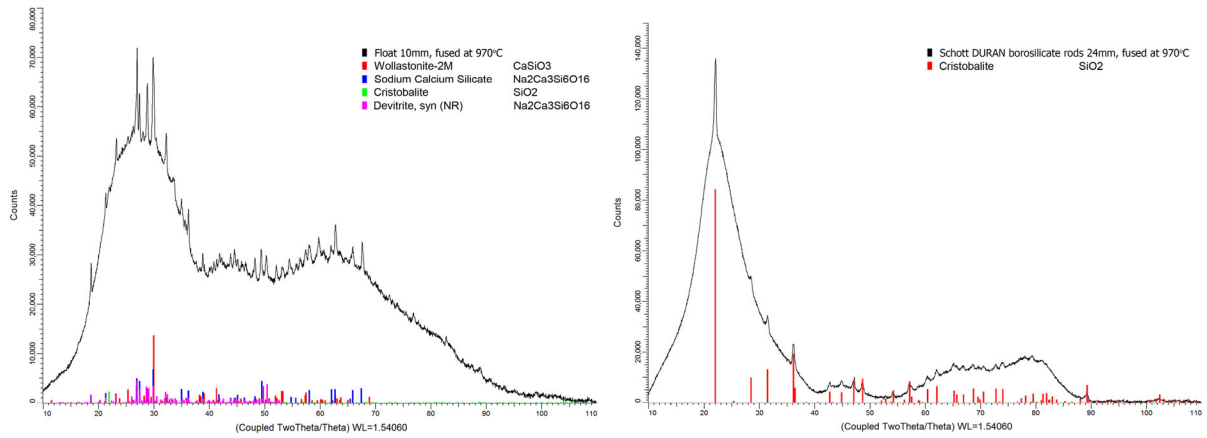


Fig. 15 XRD patterns of float glass (left) and Schott DURAN borosilicate rods (right) fused at 970 °C

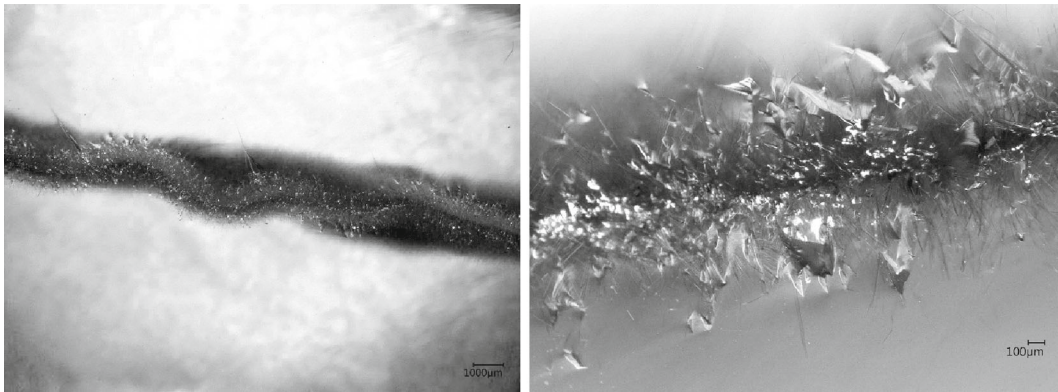


Fig. 16 Microscope images of the crystallized interface of the “Float 10mm fused 970 °C” samples (fractured surface). The parallel needle-like form of the crystals refers to devitrite

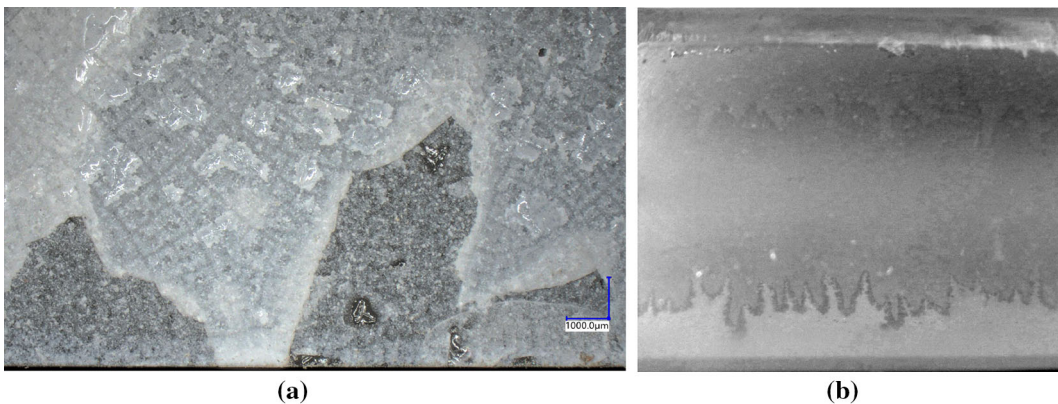


Fig. 17 Crystallized interface of the “Schott DURAN borosilicate rods, fused at 970 °C” samples. **a** Microscope image showing a split interface due to fracture. **b** Water permeability of the crystallized interface (image height \approx 30 mm)

and boron (in the case of the borosilicate glass). However, depletion of such elements may lead to unstable local compositions, as observed in the crystallized layer of the borosilicate samples, which proves porous and water-absorbing (Fig. 17). Apart from the “engineered” crystallized structures described above, the temperature conditions and fluctuations within the kiln can also provoke local and random crystallization in the form of stones, at locations of compositional alteration. Local variations in the composition can be caused by contaminants in the raw material, contact with the mould material, volatilization of compounds, and gas bubbles. Therefore, such stones are not only found in specimens produced from evidently contaminated cullet (e.g. “Car windshields” samples), but also in more pure specimens (e.g. “Fully tempered (FT)¹⁷ float” samples).

D. Reaction with mould surface.

During the kiln-casting process (at the studied viscosity range), the glass in contact with the silica/plaster investment mould, forms a thin crystallized interface, that can be easily removed by the described post-processing methodology (Fig. 18). However, of particular interest are defects caused by the interaction of the mould with the glass that are deep enough to remain upon grinding (Fig. 19). These can be, for example, stones of approx. \varnothing 1–2 mm created from loose mould material that accidentally got incorporated in the glass melt. Another characteristic flaw occurs due to the friction of the mould surface that obstructs the complete fusion between the cullet pieces. As a result, localized or networks of infolds appear at the glass surfaces, which can also encapsulate mould material. Upon grinding, the tip of these flaws may remain at the glass surface, and is observed in depths up to 5 mm. Lastly, only one case is observed where the glass bonds to the mould surface and breaks during cooling due to thermal expansion variations (sample “Borosilicate mix Maltha”).

E. Quenching rate to the annealing point.

In this study a lower quenching rate of -160°C/h is adopted in comparison to the abrupt quenching followed in industrial glass casting.¹⁸ The experimental results show that this rate is sufficient to prevent crystallization. However, attention is raised to the fact that a slower cooling rate may intensify the level of polymerization of the glass network and lead to a denser glass (Ito and Taniguchi 2004). Although this is not experimentally proven in this study, it remains a possibility to be taken into account.

F. Annealing scheme.

A conservative annealing scheme has been used, thus the residual stresses detected in the samples using cross-polarized filters are negligible and do not seem to compromise the flexural strength. Regarding the samples cut out from the standard Poesia glass bricks, these do have minor residual stresses, which is also seen by the fringe order in the isochromatic pattern obtained by an Ilis StrainScope Flex circular polariscope (Fig. 20), and also suggested strongly by the tendency of this glass to chip during post-processing.

III. Post processing.

A. Inadequate removal of existing flaws.

As also discussed at point II.D, not all surface flaws can be completely removed by post-processing (Fig. 21a). In this category of defects, the exposure during grinding of bubbles trapped in the glass bulk should be included. This results in stress concentrating semi-circular intrusions of sharp edges at the glass surface that reduce the strength. In addition, since bubbles can offer favourable conditions for the formation of crystals in their interior, the exposure of such gas-pockets at the surface bare the additional risk of stone exposure (see Figs. 19b, 21b).

B. Introduction of new flaws.

The introduction of new scratches from “rene-

¹⁷ The designation “Fully tempered” refers to the cullet used for these samples, which originates from shattered fully tempered float glass panels. The final kiln-cast components are annealed and thus not tempered.

¹⁸ In this study, quenching may last even 4 h and takes place within the kiln, which is inherently different from the quenching at atmospheric conditions during hot-pouring of glass that lasts only several minutes.

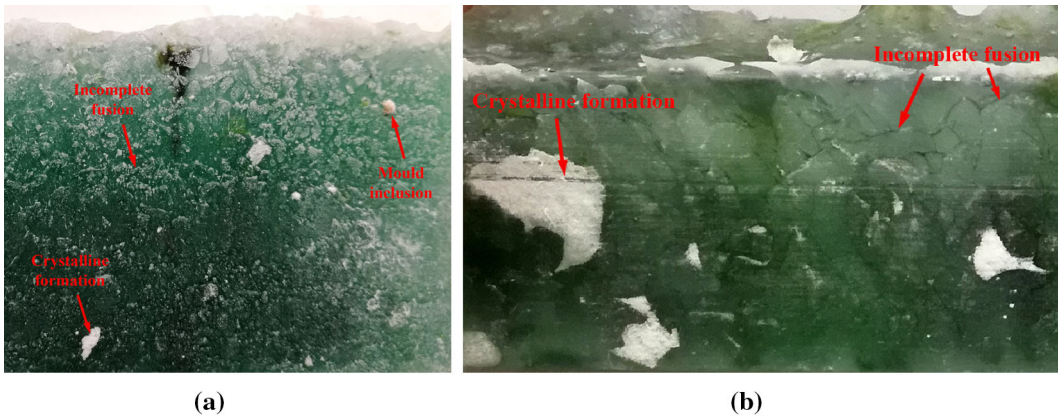


Fig. 18 Surface reaction to the mould material. **a** Side surface of a “Car Windshields, 1120 °C” sample, as released from the mould. Improper fusion of the cullet, inclusions from the mould material and stone formations are observed. **b** Side surface of an

“Oven doors, 1120 °C” specimen, as released from the mould. The white zones are crystalline formations from the reaction of the glass coating to the mould material. Improper fusion of the cullet is also observed, as well as mould material inclusions

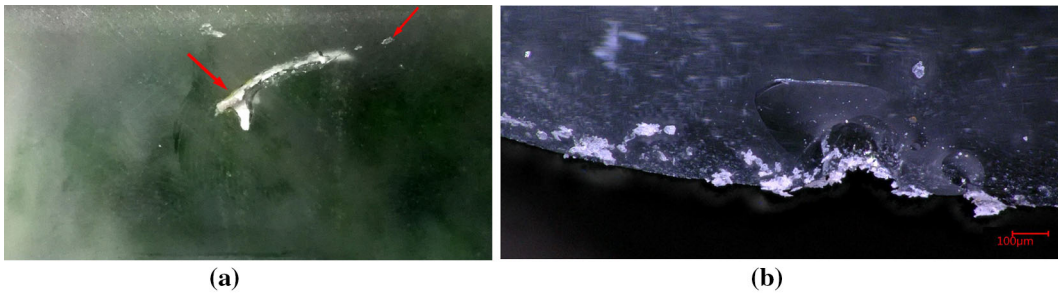


Fig. 19 **a** Infold with stone inclusions from the reaction of the glass to the mould material, in the ground surface of an “Oven doors, 1120 °C” specimen (image height ≈ 30 mm). **b** Microscope image of the fracture origin of a “Schott DURAN tubes

1120 °C” specimen. Note that the crystalline inclusion from the reaction to the mould, are not only situated at the bottom surface, but extend to the bulk as well

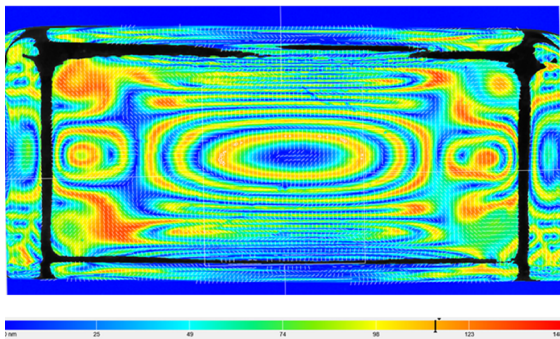


Fig. 20 Isochromic fringes observed via an Ilis StrainScoop Flex circular polariscope in a standard Poesia cast glass brick. The depth of the depicted sample is 10 cm

gade” abrasive grits (Quinn 2016) is mainly observed in glasses with lower hardness, in this study particularly the “Leerdam Lead” samples. Chipping is mainly occurring in the cut-out standard Poesia samples, as discussed in II.F. All samples present the risk of micro-cracking during coarse grinding that is not sufficiently removed in the later stages of grinding and polishing.

IV Handling.

A series of handling flaws (chippage, cleavage, percussion cone, point contact) randomly occur in some of the specimens. The response of the cast

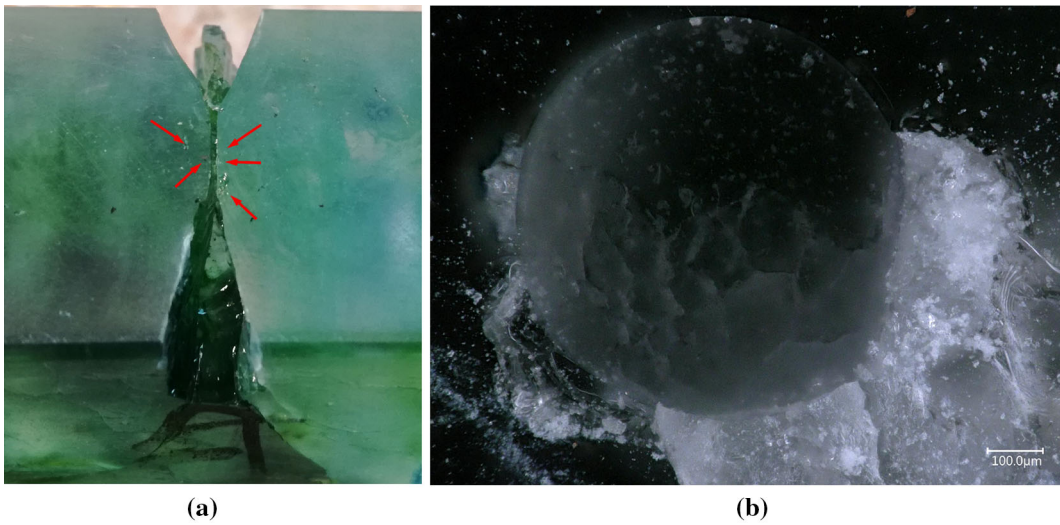


Fig. 21 **a** Clustering of surface bubbles and stone inclusions at the bottom surface of an “Oven doors, 1120 °C” specimen that were not removed after grinding, form the strength limiting

flaw. **b** Microscope image of a fractured “Schott DURAN tubes 1120 °C” specimen, showing a bubble in proximity to the surface and stone formations originating from the bubble interior

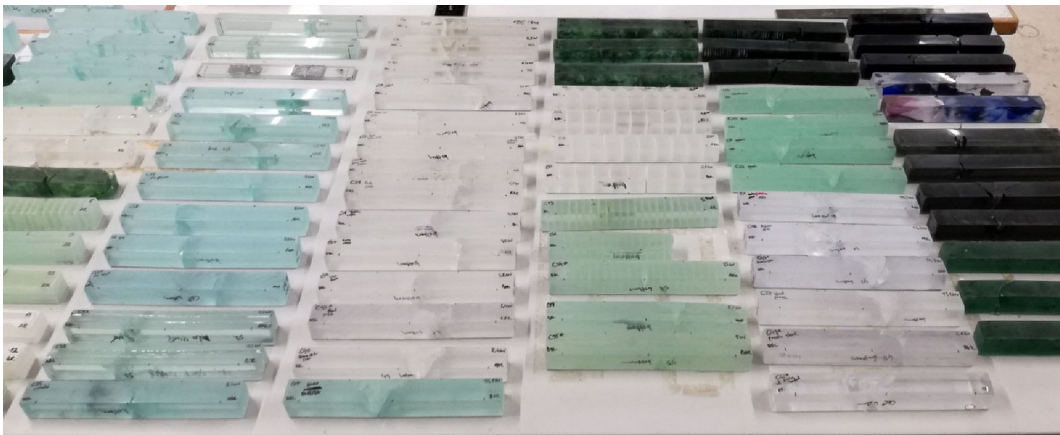


Fig. 22 Overview of tested specimens

specimens to handling damage versus that of industrially produced glass (e.g. float, extruded rods) requires further investigation, yet the more pure cast specimens are not observed to be more susceptible than standard glass products. However, attention should be drawn to the more contaminated glass samples, as occasional large defects at the surface (> 2 mm) amplify the effect of an impact.

3.2 Four-point bending tests

The results of both series of experiments are presented in Figs. 22, 23, 24, 25 and 26 and Tables 5, 6, 7 and 8. The data from the first series is mainly used for a first general guidance and as a confirmation of the second series, which is the main focus of this study. It should be stressed that the number of tested specimens per category is limited, and thus the presented results are only indicative and not sufficient for deriving statistical conclusions.

Fig. 23 Flexural strength results of 1st series of four-point bending experiments

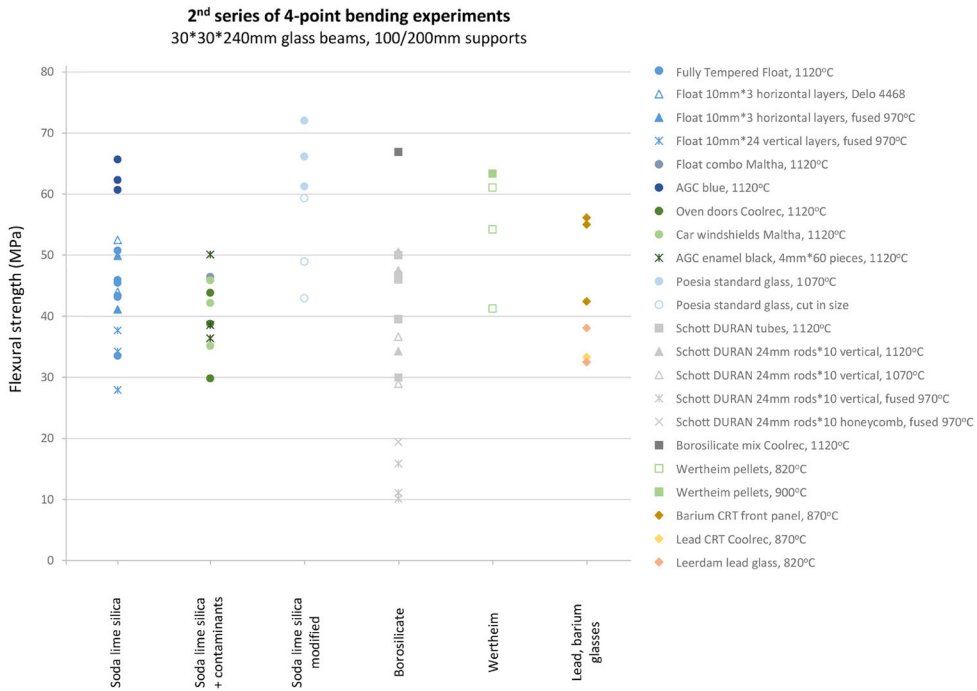
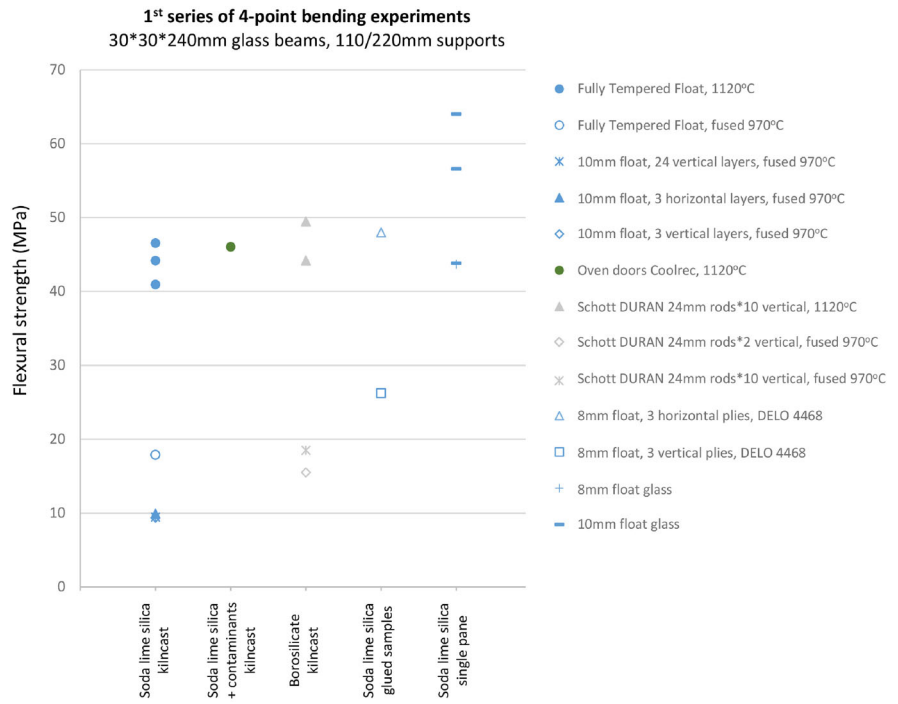


Fig. 24 Flexural strength results of 2nd series of four-point bending experiments

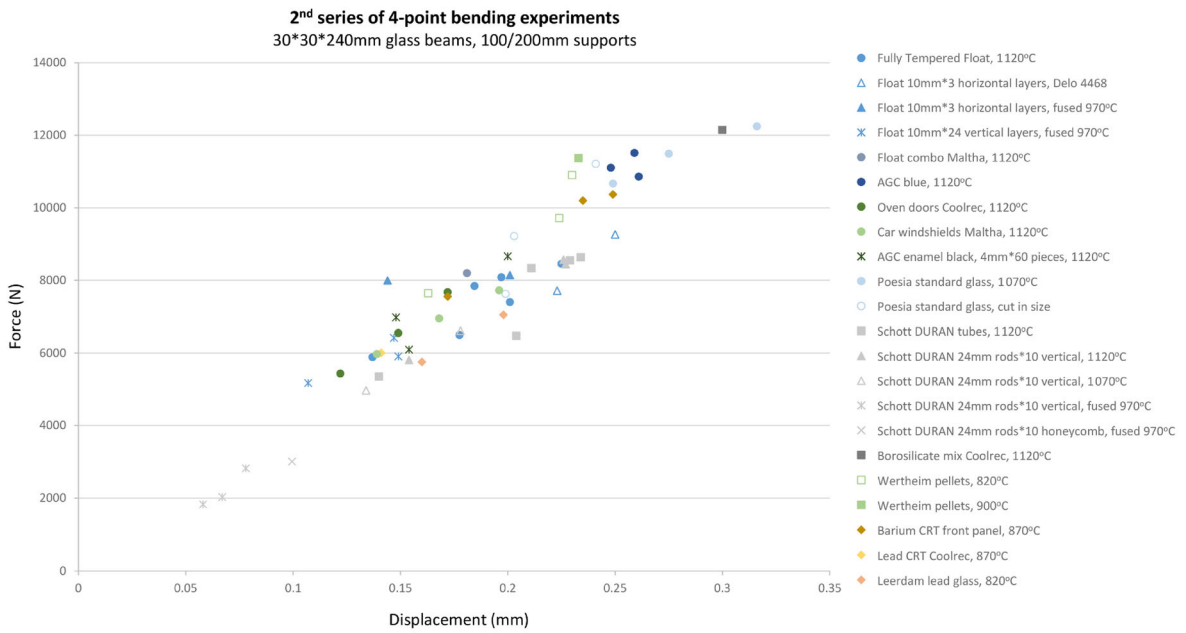
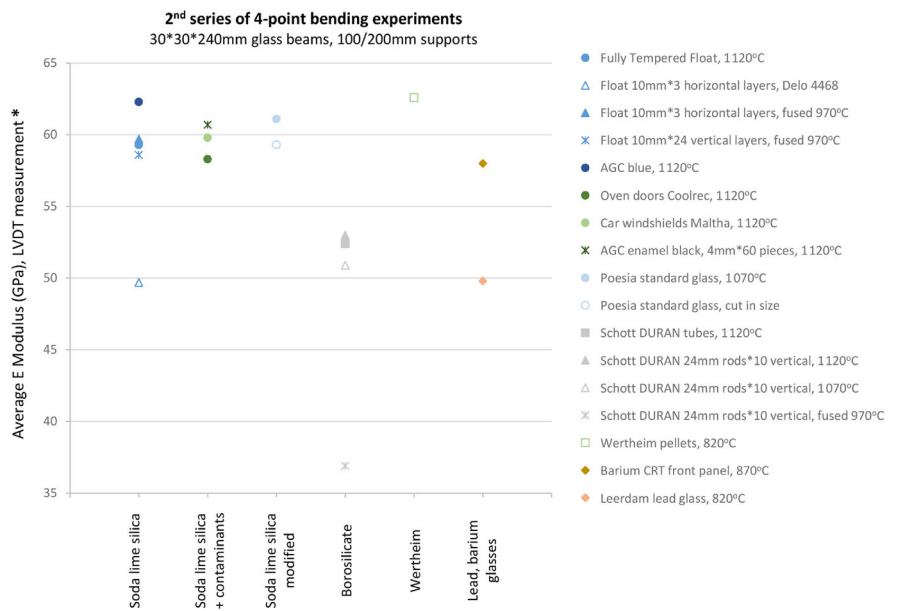


Fig. 25 Force versus Displacement graph. The displacement is measured from the DIC analysis

Fig. 26 Comparative graph of the Young’s modulus measured by the LVDT sensor during the 2nd series of four-point bending experiments



* The LVDT calculation results in a lower than expected Young’s modulus by approximately 15%, due to sensor errors. The provided data are only for comparison between the different glass types. Only glass types with more than 1 tested specimens are included in this graph

Although the first and second series differ in the fixture set-up (span, roller radius, connection detail to universal testing machine) and the sensitivity of the testing machine (10KN max. applied load for the machine used in 1st series versus 100KN for the 2nd), the results of

the two tests are aligned. More specifically, the samples of the 1st series that are cast at 1120 °C (“FT Float”, “Schott DURAN 24 mm rods”, “Oven doors Coolrec”) score within the same flexural strength range (40–50 MPa), the fused samples at 970 °C are signifi-

Table 5 Results of 1st series of four-point bending experiments concerning the kiln-cast beams

1st four-point bending experiment: Kilncast glass beams 30 × 30 × 240 mm, 110/220 mm supports						
Glass type	Specimen description	Forming temperature (°C)	No. of tested specimens	Flexural strength (MPa)		Average flexural strength (MPa)
				Minimum	Maximum	
Soda lime silica (float glass)	Fully tempered float	1120	3	40.9	46.5	43.9
	Fully tempered float	970	1	17.9		–
	Float 10 mm, 3 horizontal layers	970	1	9.5		–
	Float 10 mm, 24 vertical layers	970	1	9.9		–
	Float 10 mm, 3 vertical layers	970	1	9.4		–
Borosilicate	Oven doors	1120	1	46.1		–
	DURAN rods × 10 vertical	1120	2	44.2	49.5	46.8
	DURAN rods × 10 vertical	970	1	15.5		–
	DURAN rods × 2 vertical	970	1	18.5		–

Table 6 Results of 1st series of four-point bending experiments concerning the reference beams

1st four-point bending experiment: reference beams (240 mm length), 110/220 mm supports						
Glass type	Specimen description	Width	No. of tested specimens	Flexural strength (MPa)		Average flexural strength (MPa)
				Minimum	Maximum	
Soda lime silica	Float 8 mm, 3 horizontal layers glued with DELO 4468	30	1	48		–
	Float 8 mm, single pane	30	1	43.7		–
	Float 10 mm, single pane	50	3	43.8	64	54.8

cantly weaker (10–20 MPa) while the pure single pane float samples have a slightly better performance (average flexural strength of 55 MPa). This performance ranking and value range coincides with the results of the 2nd series apart from the case of the fused float samples at 970 °C, where a noticeably low flexural strength is reported (< 10 MPa). This is attributed to the one-off occurrence of a network of micro-cracks at the surface

of these specimens, which could not be easily removed by post-processing.

In Fig. 24, depicting the flexural strength of the second series of specimens, three main zones can be observed: specimens of a flexural strength below 30 MPa, between 30 and 55 MPa—where most samples are located, and between 55 and 75 MPa. In all specimens, crack initiation starts at the bottom sur-

Table 7 Results of 2nd series of four-point bending experiments concerning the kiln-cast beams

2nd four-point bending experiment: Kilncast glass beams 30 × 30 × 240 mm, 100/200 mm supports							
Glass type	Specimen description	Forming temperature (°C)	No. of tested specimens	Flexural strength (MPa)		Average flexural strength (MPa)	Average E modulus (GPa), LVDT calculation ^a
				Minimum	Maximum		
Soda lime silica (float glass)	Fully tempered float	1120	6	33.5	50.8	43.7	59.3
	Float 10 mm, 3 horizontal layers	970	2	41.1	49.9	45.5	59.7
	Float 10 mm, 24 vertical layers	970	3	27.9	37.7	33.3	58.6
	Float dark blue	1120	3	60.7	65.7	62.9	62.3
Soda lime silica (float glass) with contamination	Float combo	1120	1	46.5	–	–	61.8
	Oven doors	1120	3	29.9	43.8	37.5	58.3
Modified soda lime	Car windshields	1120	3	35.2	45.9	41.1	59.8
	Float with black enamel, 60 layers	1120	3	36.4	50.1	41.7	60.7
	Poesia standard cast brick	1070	3	61.3	72.1	66.5	61.1

Table 7 continued

2nd four-point bending experiment: Kiln-cast glass beams 30 × 30 × 240 mm, 100/200 mm supports						
Glass type	Specimen description	Forming temperature (°C)	No. of tested specimens	Flexural strength (MPa)		Average flexural strength (MPa)
				Minimum	Maximum	
Borosilicate	DURAN tubes	1120	5	30	50	42.5
	DURAN rods × 10 vertical	1120	3	34.3	50.6	44.1
	DURAN rods × 10 vertical	1070	3	24.5	36.7	30
	DURAN rods × 10 vertical	970	3	10.1	15.9	12.4
Wertheim (C-glass)	DURAN 24-mm rods, honeycomb	970	1	19.4	–	–
	Borosilicate mix Cooltec	1120	1	66.9	–	–
Barium–strontium silicate	Wertheim pellets	820	3	41.3	61.1	52.2
	Barium CRT front panel	900	1	63.4	–	–
Potash–lead silicate	Lead CRT funnel	870	3	42.4	56.1	51.2
	Lead glass	820	2	33.3	38.1	35.3

^aThe LVDT calculation results in a lower than expected Young's modulus by approximately 15%, due to sensor errors. The provided Young's modulus data are only for comparison between the different glass types

Table 8 Results of 2nd series of four-point bending experiments concerning the reference beams

2nd four-point bending experiment: reference beams 30 × 30 × 240 mm, 100/200 mm supports						
Glass type	Specimen description	No. of tested specimens	Flexural strength (MPa)		Average flexural strength (MPa)	Average E modulus (GPa), LVDT calculation ^a
			Minimum	Maximum		
Soda lime silica	Float 10mm, 3 horizontal layers glued with Delo 4468	2	44	52.5	48.3	49.7
Soda lime potash borosilicate	Poesia standard cast glass brick, cut & polished	3	42.9	59.3	50.4	59

^aThe LVDT calculation results in a lower than expected Young's modulus by approximately 15%, due to sensor errors. The provided Young's modulus data are only for comparison between the different glass types

Fig. 27 Side view of kiln-cast specimens fractured during the 2nd series of four-point bending tests. Note that the primary crack starts perpendicular to the beam's long axis and then splits in the case of medium/large accumulated elastic energy (prior to cracking), or propagates as one crack in the case of low energy (e.g. crystallized specimens). At the top (compressive zone), the crack forms compression curls



face (or at very close proximity), at the area between the support pins (zone of maximum tensile stress, see Figs. 27, 28). As a general trend, glass specimens produced at lower viscosities and from purer cullet are found at the top zone of the flexural strength graph, while specimens with obvious strength-limiting flaws exposed at the bottom surface fail at low values.

An overview of the main fracture origins is presented in Fig. 29, summarizing the most critical defect cate-

gories: stones, crystalline interfaces, surface bubbles, and machining damage. The size of the fracture mirror is measured in a selection of specimens (Fig. 30) and plotted against the flexural strength σ (Fig. 31) based on "Orr's equation" (Quinn 2016):

$$\sigma = \frac{A}{\sqrt{R}} \quad (7)$$

where R corresponds to the mirror radius (in this study the mirror size extending to the mist-hackle boundary at

Fig. 28 Graph depicting the location of the fracture origin of the 2nd series specimens at the bottom surface. Note that fracture origins found at the two long edges are usually related to machining flaws

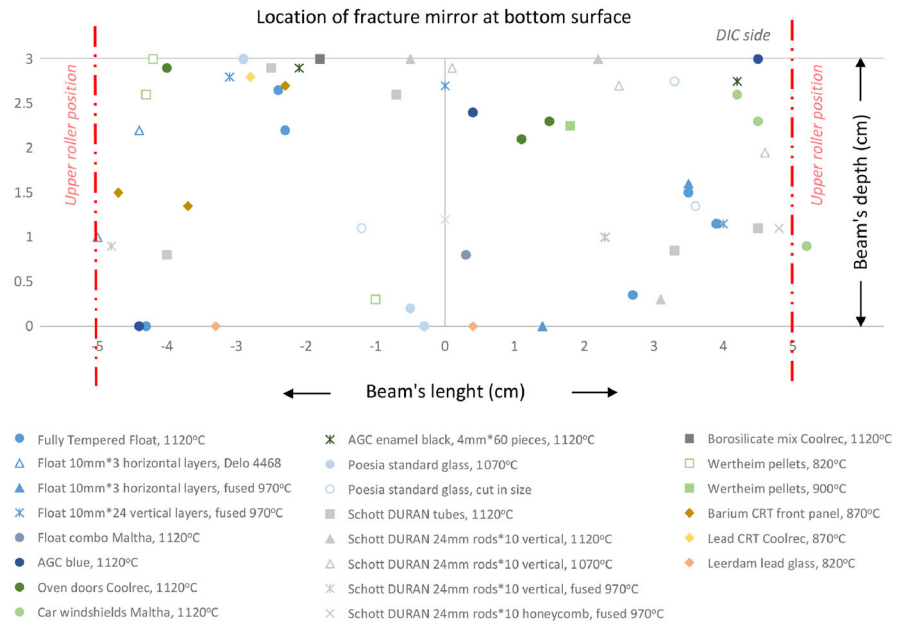
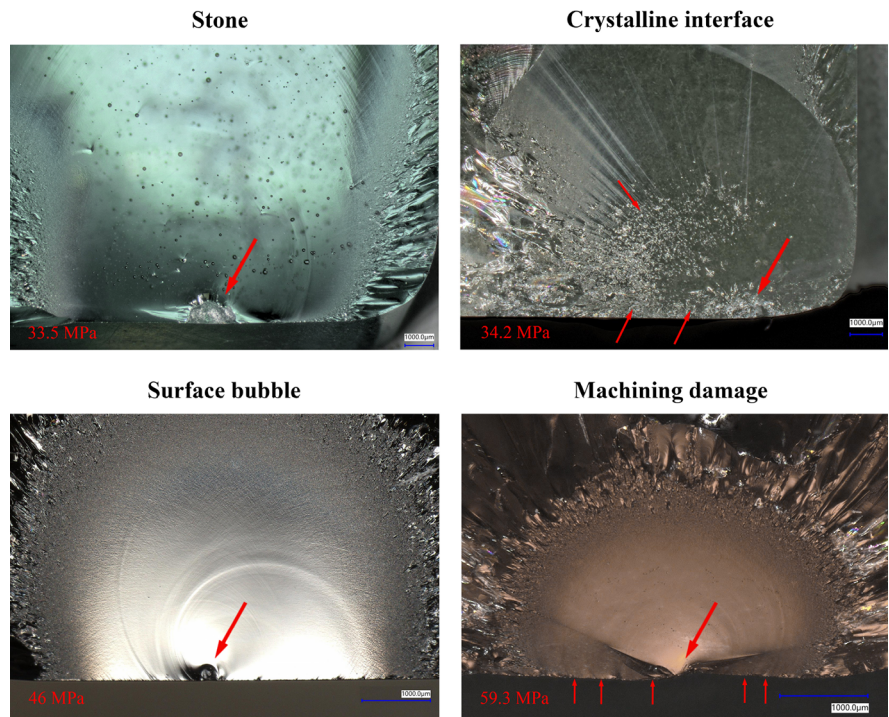


Fig. 29 Mirror surfaces of fractured specimens (2nd series of experiments) depicting the main defect categories responsible for catastrophic failure. The reported flexural strength is linked to the type of defect but also to its size



the bottom surface of maximum tension is measured) and A is the characteristic mirror constant per glass composition.

Typically, the larger the failure stress is, the smaller the encountered fracture mirror will be. The increase

of the width of the critical flaw is, as expected, responsible for the decrease of the flexural strength (Fig. 32). The higher strength specimens seem to fail mainly from machining flaws, whereas stones or crystalline interfaces are responsible for the fracture of the lower

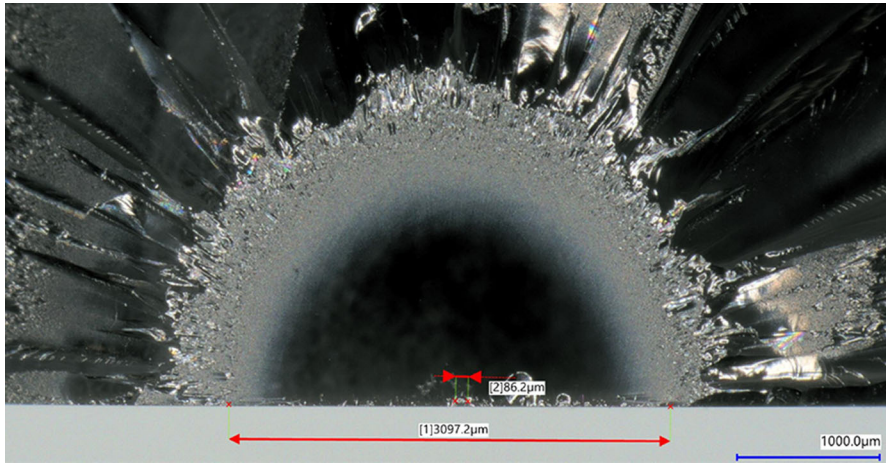


Fig. 30 Measuring example of the fracture mirror and defect size at origin. All measurements are conducted employing a Keyence VHX-7000 Digital Microscope and with the fractured surface positioned perpendicularly to the microscope’s optical path. To obtain the mirror radius, the diameter of the mist-hackle boundary at the bottom surface line (maximum tensile stress) is measured and then divided by half. This method is chosen as not all mirrors are found semi-circular. More specifically, due to the

stress gradient along the height of the sample (due to loading in bending), the mirrors appear elongated in this direction, or may even be incomplete. Therefore a measurement along the bottom surface is preferred. Moreover, extended flaws at the surface or machining damage can cause the one-sided elongation of the mirror, and thus the measurement of the diameter instead of the radius is opted

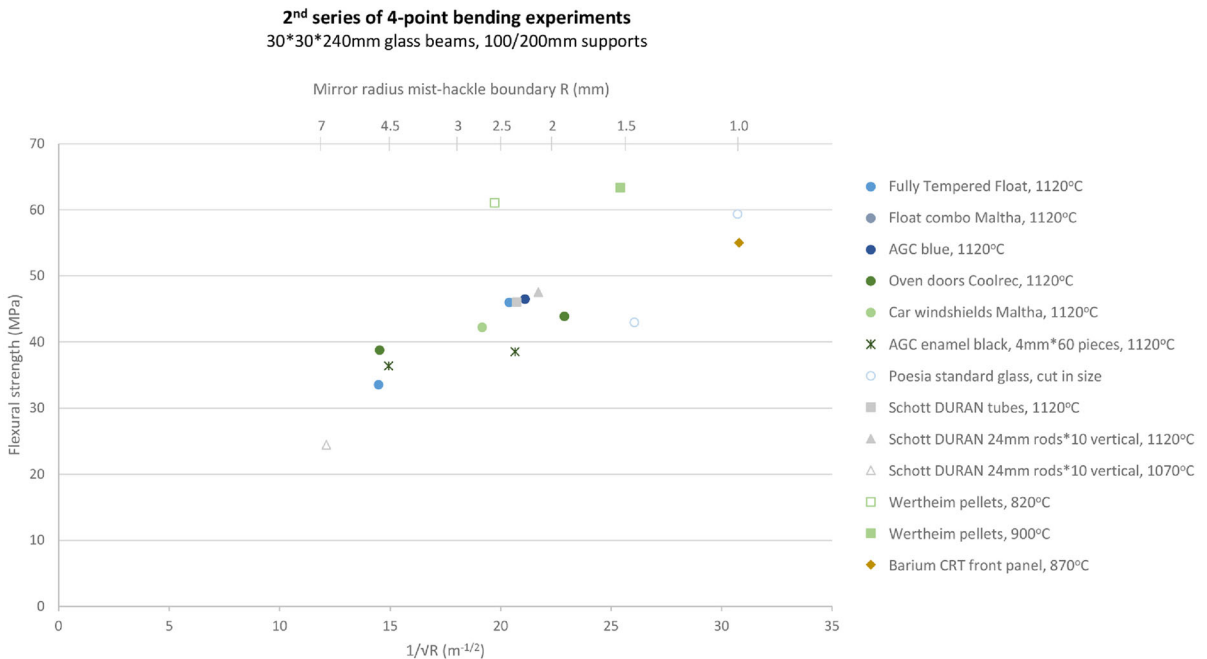


Fig. 31 Flexural strength versus $1/\sqrt{R}$ graph for a selection of glass specimens. In general, the higher the strength, the smaller the mirror size. However, since the mirror size to strength rela-

tionship of different glass compositions is reported, more than one mirror constants A are applicable, and thus the data are not all corresponding in one line (e.g. “Wertheim pellets” samples)

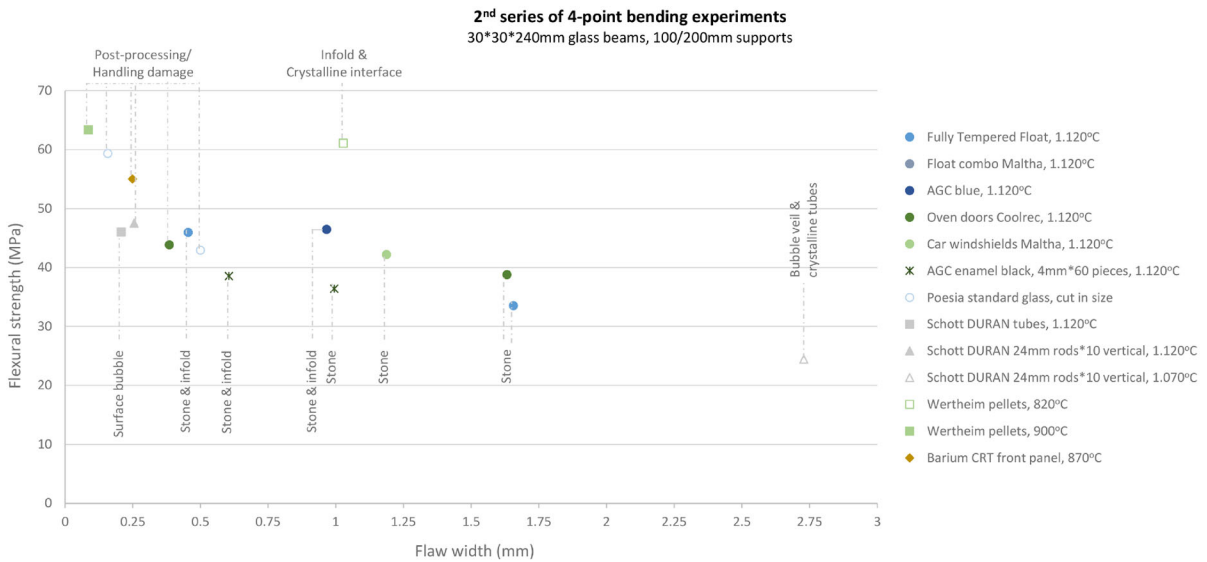


Fig. 32 Flexural strength versus critical flaw width (at fracture origin) for a selection of glass specimens. The strength reduces with the increase of the flaw size, and specimens with surface

stones tend to fail at lower strength values than the purer samples that fail from post-processing and handling flaws

strength specimens. Yet, the type, size, quantity and location of flaws alone cannot justify why some glass samples score lower than others. The structural performance of each glass type needs to be reviewed as conjointly dependent on the chemical composition of the glass as well as its inherent defects (see Sect. 4). Also, fracture load uncertainty may be applicable due to environmentally assisted slow crack growth (Quinn et al. 2009), as the applied loading rate is slower (approx. by half) than the suggested rate by the ASTM C158-02 guideline. The effect of slow crack growth should be further experimentally investigated in a broader range of testing speeds.

Regarding the Young’s modulus, the calculation conducted based on the LVDT data results in values that are approximately 15% lower than those found in literature. This is considered a systematic error and is attributed to the quality of the sensor. However, in each triplet of tested glass type, there are matching E values reported. In addition, the stiffness relationship between the different glass families (Fig. 26) is found in accordance with the literature (Corning 1979; Campbell and Hagy 1975), and specifically:

$$E_{\text{Potash Soda Lead-silicate}} \leq E_{\text{Borosilicate}} < E_{\text{BaO/SrO-Silicate}} < E_{\text{Soda Lime Silica}}$$

4 Discussion

The flexural strength of the cast glass specimens is conjointly related to their chemical composition and inherent defects. To comprehend in which cases the flaws are the strength limiting factor and when the mechanical properties related to the composition have a determining role, the interpretation of the results is structured in the following categories: a. Non-contaminated glass specimens, b. Contaminated vs. non-contaminated glass, c. Non-contaminated homogeneous glass specimens vs. with crystallized interfaces, and d. Reference specimens. In this manner, the defects are categorized and isolated so their effect can be studied with more clarity, while the absence of overruling flaws (in the case of the pure samples) highlights the effect of the chemical composition.

(a) Non-contaminated glass specimens

The purest, most homogeneous samples of each glass family included in this work are selected for comparison (Figs. 33, 34). As these examples contain less imperfections, the effect of their chemical composition on their flexural strength is highlighted. Table 9 lists relevant calculated and/or measured physical and mechanical properties of these glasses, along with data found in literature for similar compositions.

Fig. 33 Average flexural strength to Young’s modulus graph concerning the non-contaminated kiln-cast specimens of the 2nd series

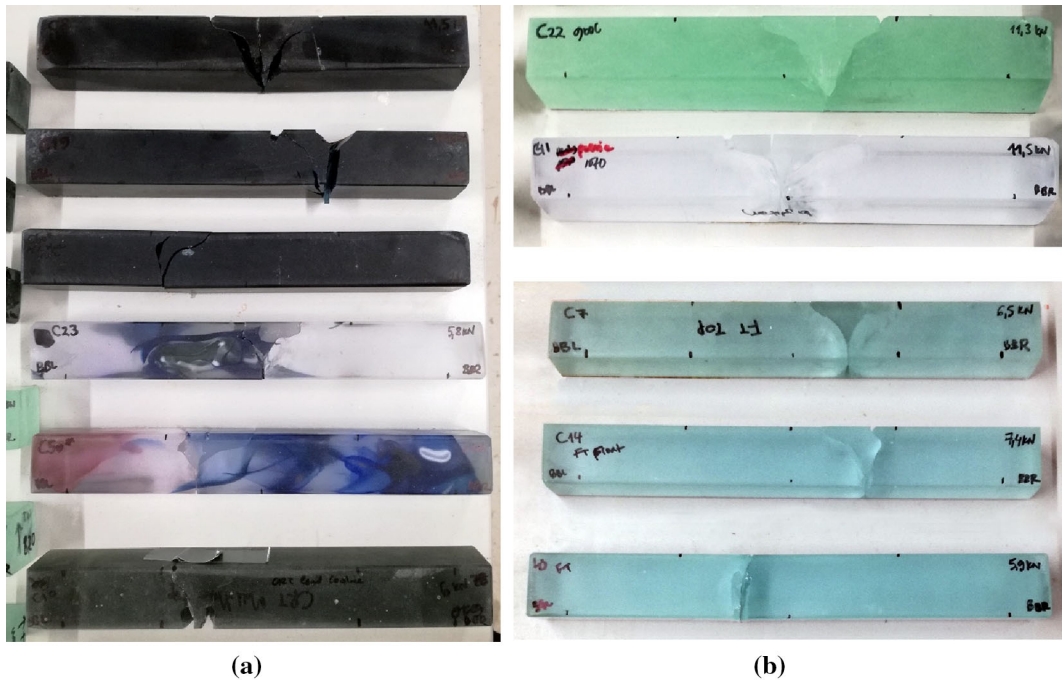
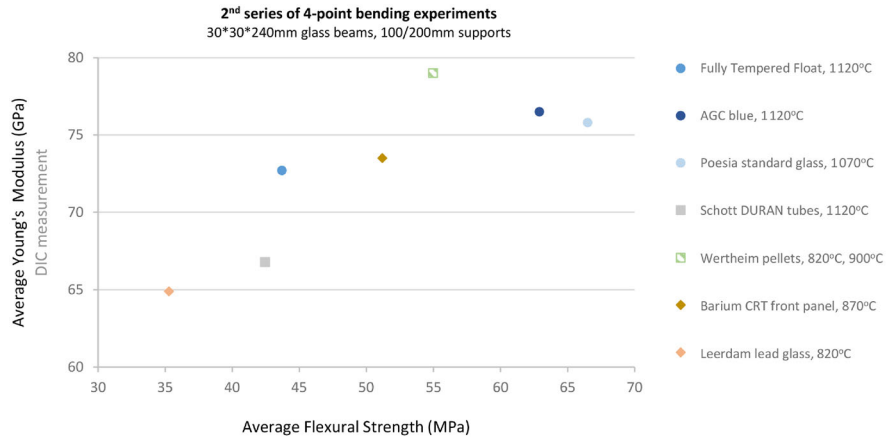


Fig. 34 Side surface of fractured specimens. **a** First three specimen correspond to “AGC dark blue float 1120 °C” glass, then the next two are “Leerdam 820 °C”, followed by a “Barium CRT

870 °C” glass. **b** From top to bottom: “Wertheim 900 °C”, “Poesia 1070 °C” and three “FT Float 1120 °C” specimens

Therefore, although the LVDT calculation does not provide exact values, it can be reliably used for a comparative analysis between the different glass types. The DIC measurement is utilized to provide more accurate data regarding the maximum deformation, and for performing more precise calculations of the E moduli for a selection of glass samples (see Sect. 4a). Nonetheless, the coupling of the DIC measurement during 4-point bending with a non-destructive testing method for determining the E modulus, such as the Impulse Exci-

tation Technique, is advised in future testing, to verify the reliability of the results.

As seen in Fig. 33, there is an increase in the flexural strength with increasing Young’s modulus,¹⁹ in the lead silicate, borosilicate, barium silicate and AGC

¹⁹ The graph in Fig. 33 is based on the Young’s modulus calculated from the DIC measurements. The reported E modulus is approximately 5% higher than in literature, which could be partly related to testing errors and partly to the material itself and its casting procedure.

Table 9 Measured and calculated properties of the selected (pure) glasses (in bold), and reference glasses of similar composition

Glass type	Name	Composition (wt%)											BaO	SrO	Source		
		SiO ₂	B ₂ O ₃	Na ₂ O	K ₂ O	CaO	MgO	Al ₂ O ₃	PbO	Fe ₂ O ₃	Sb ₂ O ₃	ZnO					
Soda lime silica	Standard float	70–74		12–16	0–0.5	8–13	0–5	0–2		0.01–1.5						[1]	
	PPG Starphire (low iron)	74.6		13.3		8.9	3	0.04								[5]	
	FT Float	75.4		12.4		7.6	4	0.4		0.09						[5]	
	AGC blue	73.1		12.8		8.1	4	0.9		0.76						[5]	
	Poesia glass	72.1	2.5	15.9	1.9	6.1	0.06	0.3		0.9						[5, 8]	
Modified Soda Lime	Coming 7740	80.6	13	4				2.3								[9]	
	Pyrex																
Borosilicate	Schott DURAN	81	13	4				2								[11]	
	Johns Manville 753 C-glass fibers	63.5	5.5	14.6	1	6	3	5.5		0.1						[14]	
	Wertheim glass	63.8	5.5	11.8	3.2	6.4	3.7	5.2		0.06				0.08		[5, 14]	
SiO/BaO Silicate	Coming 9068	63.2		7.1	8.8	1.8	0.9	2		2.3			0.4		2.4	10	[17]
	Philips CRT panel	61.6		7.2	6.8	1.1	0.3	2.3		0.1					8	8	[5]
Potash-lead-silicate	Coming 0120	55	3	4	9			2		27							[18]
	Leerdam glass	57.7		3	9					28.7			0.8		0.6		[5]
Glass type	Name	Annealing point 10 ³ dPa s (°C)	Density (g/cm ³)	Poisson's ratio	Knoop's Hardness KHN100	Molar volume V _m (cm ³ /mol), calculated	APF calculated based on Pauling's ionic radii	G _i Total Dissociation energy (kJ/cm ³), calculated ^b	E (GPa), calculated	E (GPa) from literature	E (GPa) from LYDVT measurement ^{**}	E _i (GPa) from DIC measurement ^{***}	Average Flexural Strength (2nd 4-PB test) (MPa)				
														E (GPa) from literature	E (GPa) from LYDVT measurement ^{**}	E _i (GPa) from DIC measurement ^{***}	Average Flexural Strength (2nd 4-PB test) (MPa)
Soda lime silica	Standard float	525–545 [3]	2.480–2.520 [1]	0.22–0.23 [1]	550 [4]					70–75 [2]							
	PPG Starphire (low iron)	547 [4]	2.510 [4]	0.22 [4]	448 [4]	23.55	0.5492	64.03	70.33	73.1 [4]							
	FT Float	553 [6]	2.466 [7]			23.92	0.5413	64.84	70.19		59.3			72.7		43.71	
	AGC blue	550 [6]	2.492 [7]			23.81	0.5436	64.87	70.52		62.3			76.5		62.9	
	Poesia glass	≈ 520 [6]	2.486 [7]			24.65	0.5471	61.84 (IV) ^c	67.67 (IV) ^c		61.1			75.8		66.5	
Modified Soda Lime	Coming 7740	560 [10]	2.230 [10]	0.20 [10]	418 [10]					64 [10]							
	Pyrex																
	Schott DURAN	560 [12]	2.230 [11]	0.20 [11]	480 [13]	27.53	0.5383	64.13 (B ₂ O ₃ 66%, III, 34% IV)	69.04 (B ₂ O ₃ 66%, III, 34% IV)	63 [11]	52.4			66.8		42.45	

Table 9 continued

Glass type	Name	Annealing point 10^{13} dPas (°C)	Density (g/cm ³)	Poisson's ratio	Knoop Hardness KHN100	Molar volume V_m (cm ³ /mol), calculated	APF calculated based on Pauling's ionic radii	G_i Total Dissociation energy (kJ/cm ³), calculated ^b	E (GPa), calculated	E (GPa) from literature	E (GPa) from LVDT measurement ^c	E (GPa) from DIC measurement ^{ccc}	Average Flexural Strength (2nd 4-PB test) (MPa)
C-Glass	Johns Manville 753 C-glass fibers	527 [14]	2.520 [16]	0.27 ^a [15]			0.5586	66.01 (IV) ^c	73.74 (IV) ^c	68.9 ^a [15]			
	Wertheim glass	550 [6]	2.502 [7]			24.56	0.5555	66.38 (IV) ^c	73.75 (IV) ^c	63.6	79		54.98
SrO/BaO Silicate	Corning 9068	503 [17]	2.696 [16]				0.5456	61.00	66.56				
	Philips CRT panel	530 [6]	2.766 [7]			25.24	0.55	62.22	68.20	58	73.5		51.19
Potash- Lead- Silicate	Corning 0120	435 [10]	3.050 [10]	0.22 [10]	382 [10]		0.5484	60.17 (IV) ^c	65.99 (IV) ^c				
	Leerdam glass	465 [6]	3.031 [7]			26.5	0.5288	58.35	61.71	49.8	64.9		35.29

Sources

[1] Quinn and Swab (2017)
 [2] Shelby (2005)
 [3] Marijnsen and Warimont (2005)
 [4] Specialty Glass Products
 [5] XRF measurements conducted by Ruud Hendriks
 [6] Calculated using viscosity model by Fluegel (2007a)
 [7] Calculated using density model by Fluegel (2007b)
 [8] Personal correspondence with Poesia
 [9] Friedrich & Dimmock Inc.
 [10] Corning (1979)
 [11] Schott (2015a, b)
 [12] Schott (2017)
 [13] Abrisa Technologies (2014)
 [14] Campbell and Hagy (1975)
 [15] Matweb
 [16] ASM International (1995)
 [17] Thompson (1980)
 [18] Gregory (1998)

^aProperties corresponding to a generic c-glass fiber

^bCalculated based on data from Inaba et al. (1999)

^c(III) Corresponds to B₂O₃ with coordination number = 3, (IV) to B₂O₃ with coordination number = 4. The coordination number ratio for the Schott DURAN glass is calculated using the formulas proposed by Yun and Bray (1978). For the Poesia, Wertheim and Corning 0120 glass, a 100% fourfold coordination is assumed given the high alkali/boron ratio (Priven 2000; Zhdanov and Shmidel' 1975).

[^]Calculated using V_i values from Makishima & Mackenzie (1972), and G_i values from Inaba et al. (1999)

[~]The LVDT calculation results in a lower than expected Young's modulus by approximately 15%, due to sensor errors. The provided data are only for comparison between the different glass types.

^{ccc}The reported E modulus is approx. 5% higher than in literature, partly due to testing errors and partly due to the material itself and its casting procedure

dark blue float glass samples. The increase in strength is attributed to the increase of the average bond strength and atomic packing density of the glass network. This is related to the Young's modulus by the equation below (Makishima and Mackenzie 1973):

$$E = 2 \cdot C_g \cdot G_t \quad (8)$$

where C_g is the atomic packing density (also mentioned as Atomic Packing Factor, APF), and G_t the total dissociation energy per unit volume. Based on the chemical compositions derived by the XRF analyses, the APF²⁰ and G_t ²¹ are calculated and listed in Table 9.

Therefore, by reviewing Table 9, it is anticipated that the lead silicate glass samples, which present the lowest dissociation energy and packing density, will have the lowest strength as well,²² while the soda lime

²⁰ The atomic packing density is calculated using the following formulas:

$$APF = \frac{\sum x_i \cdot V_i}{V_m} \quad (9)$$

where x_i is the molar fraction, V_i the ionic volume of the i th oxide and V_m is the molar volume of glass, and specifically:

$$V_i = \frac{4}{3} \cdot \pi \cdot N_A \cdot (x \cdot r_A^3 + y \cdot r_B^3) \quad (10)$$

and

$$V_m = \frac{M}{\rho} \quad (11)$$

where N_A is the Avogadro's number, $r_{A,B}$ = ionic radii of M_xO_y oxide, M is the molecular mass and ρ is the density of the glass. The V_i is derived from Makishima and Mackenzie (1973) and Inaba et al. (1999) based on Pauling's ionic radii. The density is calculated from the chemical composition using the model developed by Fluegel (2007b).

²¹ The total dissociation energy is calculated from the dissociation energy of the oxide constituents listed in the work of Inaba et al. (1999).

²² PbO has one of the lowest G_i as reported by Makishima and Mackenzie (1973), and a relatively high molar atomic mass. The increased mass of the lead ion slows down the chemical reactions during quenching, and results in a less organized/packed network.

silicate (SLS) glasses will have the highest strength. Also in accordance with the literature, the BaO containing silicate glass has a lower flexural strength and Young's modulus than the CaO silicates but higher than the lead silicates (Volf 1984; Corning 1979). However, the Young's modulus alone cannot justify the deviation from the linear E/strength relationship that present the Poesia, Wertheim, and FT float glass samples, and further explanation is required per glass type.

The Poesia glass is a modified soda lime glass with a decreased forming temperature compared to conventional float glass (T_L is at around 980 °C, therefore 80–100 °C lower than for SLS). It contains K_2O and B_2O_3 in small amounts (< 3 wt%), and has a higher Na_2O/CaO ratio than typical SLS recipes. Despite the slightly lower E modulus²³ than the one of AGC dark blue glass, it presented the highest flexural strength among all tested specimens. This is attributed to a lower brittleness of this particular glass. Sehgal and Ito (1998) state that a higher molar volume (V_m) plays a key role in the reduction of the brittleness, as a more open structure allows more deformation prior to crack initiation. More specifically, an increasing soda/calcia ratio would decrease the brittleness, as well as the partial substitution of soda for potash. This is in accordance with the compositional variations of Poesia glass to the typical SLS recipe, which contribute to a more open structure (Fig. 35) that allows for a slightly increased accommodation of the stresses around the point/flaw where the crack will initiate. The "Poesia 1070 °C specimens failed due to machining damage (Fig. 36).

The Wertheim glass has the highest measured Young's modulus and the highest calculated total dissociation energy, while it's calculated molar volume is similar to the Poesia glass. The higher stiffness (in comparison to an SLS glass) can be attributed to the partial substitution of silica with alumina ($\approx 5\%$), that reduces the openness of the network Sehgal and Ito (1998). Similar to the Poesia glass, it has a lower forming temperature than SLS glasses (T_L at around 1015 °C), which

²³ It should be noted that the calculated E_{Poesia} using the APF and G_t corresponding to the chemical composition is found much lower than the $E_{AGC\ blue}$. This could be related to a wrong estimate of the B_2O_3 content, which cannot be determined by the XRF analysis, and/or a higher packing density attributable to the thermal history of the kiln-cast components. The E_{Poesia} derived from the LVDT data is thus considered more reliable for further analysis.

Fig. 35 Graph of total dissociation energy versus the molar volume

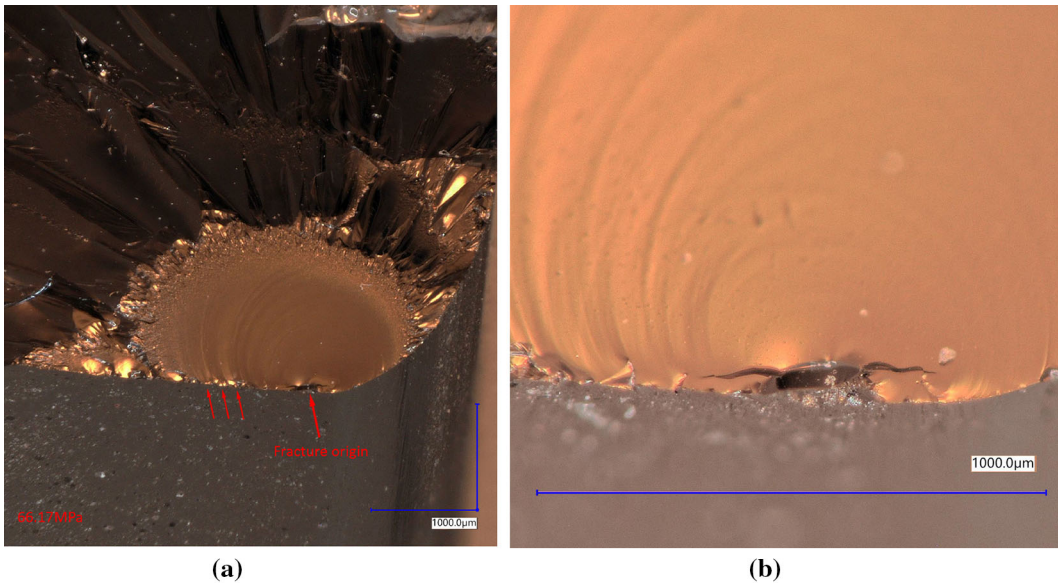
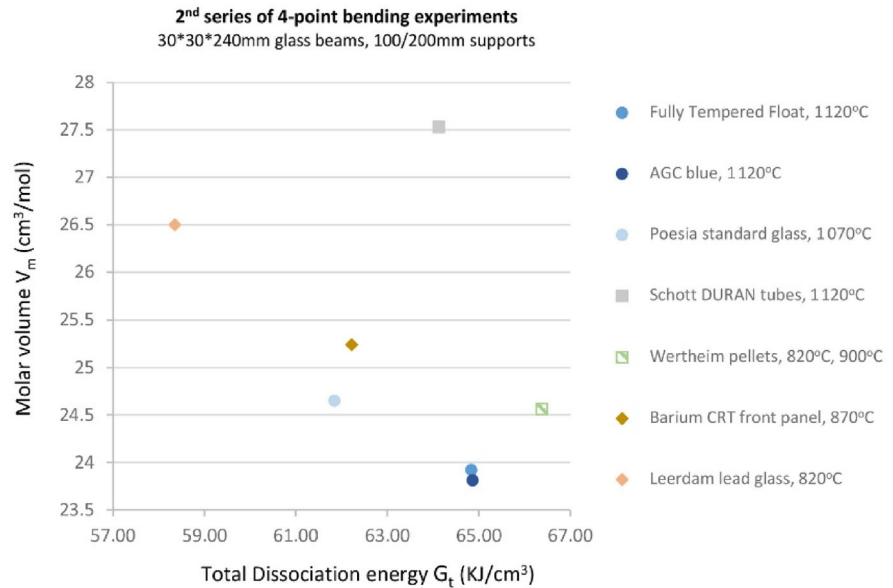


Fig. 36 a Microscope image of the bottom surface and corner, and the fracture surface of a “Poesia 1070 °C” specimen. The cause of failure is grinding damage, which is demonstrated by

the fracture mirror elongation to the left and the consecutive machining crack hackles along the fractured edge. **b** close-up of the fracture origin

can be linked to the mixed alkali effect²⁴ and the presence of boron trioxide in a small quantity (Morey 1932). According to the E/V_m properties of this glass, a much higher flexural strength should have been expected. The

²⁴ The term describes anomalies observed in glasses and melts containing a mixture of two or more alkali oxides. According to Shelby (2005), the viscosities of such melts are lower than those containing the same amount of a single alkali oxide.

reason this glass failed at a lower stress is linked to its kiln-casting at temperatures (820 °C, 900 °C) well below its liquidus point, which resulted in evident inhomogeneities. These inhomogeneities are concentrated in the interface created between each pellet of glass, and compose a 3-dimensional network of planar zones consisting of bubbles and loose crystal formations. In addition, the forming temperature favours the occur-

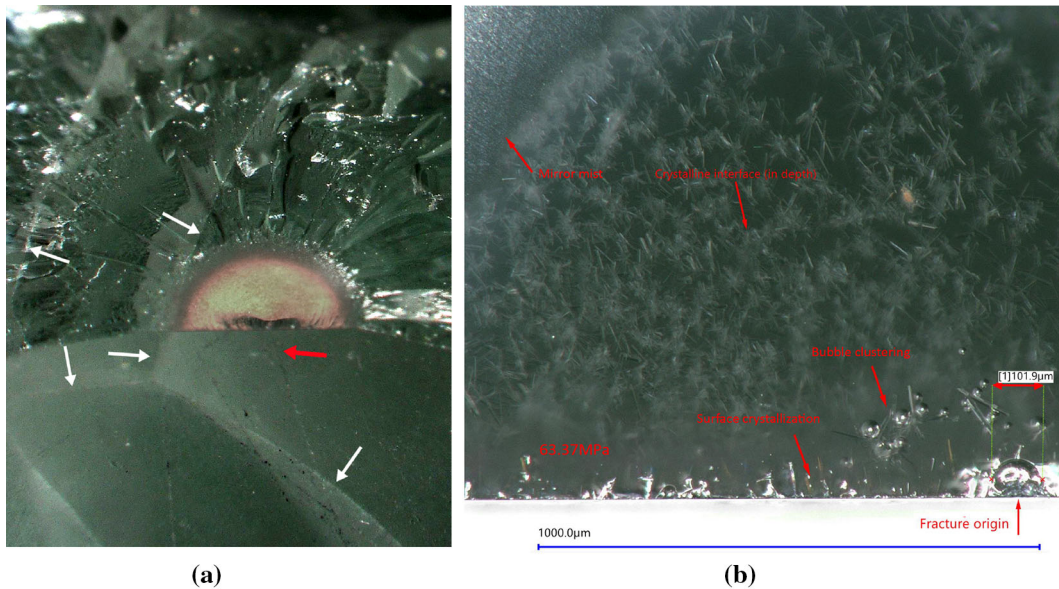


Fig. 37 Fracture surface of the “Wertheim 900 °C” specimen. **a** Microscope image showing the bottom surface and fracture mirror. The specimen failed from a grinding scratch (red arrow) next to the fusion interface (white arrows). **b** Close-up of the mir-

ror and the crystalline interface located just below the fractured surface (only the crystal formations along the bottom surface are fractured)

rence of stones, due to the reaction of the hot glass with the mould, which are sufficiently sub-surface that they cannot be entirely removed during standard post-processing. These stones seem to weaken the glass surface and contribute to the formation of deeper striations during grinding, which are the sources of failure. The above described 3D network may not be responsible for the crack origin, but given that the specimens fail from a flaw in close proximity to the network, it may contribute to zones of concentrated stress along the surface (Fig. 37).

It is also interesting to compare the “AGC dark blue float” to the “FT float” specimens. These two glasses have very similar compositions and are almost identical in calculated atomic packing density and total dissociation energy. However, the measured Young’s modulus of the “FT float” glass specimens is lower, and so is the flexural strength. This is probably linked to the thermal history of these two glasses. On the one hand, the “AGC dark blue” glass has a slightly lower liquidus point (T_L is around 1046 °C, while for the “FT Float” is 1063 °C). On the other hand, the dark colour of the AGC glass seems to contribute to the quality of the casting. The dense dark blue colour absorbs more infra-red light during heating than the transparent light blue, thus the body

will heat up faster. In a similar manner, the dark glass will set faster during cooling due to the greater heat loss by radiation (Kitaigorodskii and Solomin 1934; Burch and Babcock 1938). The faster setting rate can influence the coordination state of the transition metal oxides included in the composition²⁵ and thus affect the total dissociation energy of the network bonds—something not accounted for in the calculations. In addition, the lower liquidus point and increased heat absorption promote the full fusion of the cullet pieces and the elimination of stone formation, thus leading to the diminishing of flaws at the glass surface, and to a higher flexural strength. In antithesis, infolds at the glass surface of the “FT float” specimens are created by insufficient fusion of the cullet positioned next to the mould walls, and crystalline inclusions due to contamination from the mould, are the main cause of failure of the “FT float” samples, according to the analysis of the fracture mirrors (Fig. 38). Due to these flaws, the “FT float” glass specimens fail at values lower than expected in comparison to the rest of the samples.

²⁵ The XRF identifies a series of transition metals in this glass that act as colorants: 0.76% Fe₂O₃, 0.065% TiO₂, 0.029% MnO, 0.023% Cr₂O₃).

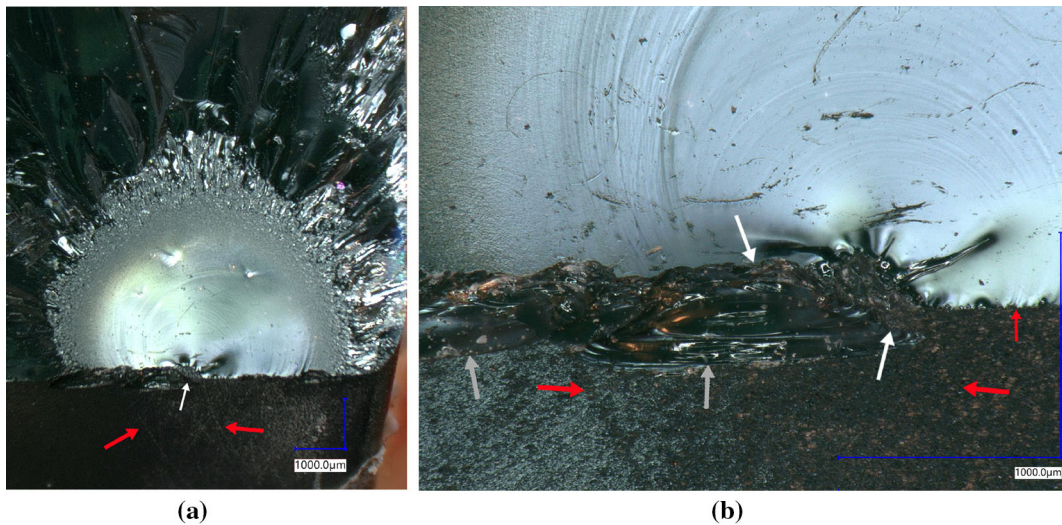


Fig. 38 Microscope images of the bottom and fracture surface of a “FT Float 1120 °C” specimen, showing the fracture origin (Fig. 38b is a magnification of the fracture origin). The cause of failure is a combination of grinding scratches (red arrows) acting upon a surface infold with crystalline inclusions (white arrows).

The hertzian cones (grey arrows) that refer to impact damage have an opposite to the crack front direction and are considered secondary breaks. Looking through the hertzian cones, traces of crystalline inclusions can be observed

Regarding the fracture analysis of the glasses studied in this category, the most prevailing causes of failure are found to be machining damage and handling flaws (see also Fig. 28, most “pure” specimens fail at an edge flaw), justifying that the purity of the cullet and the relatively high forming temperatures (in comparison with other glass samples in this work) eliminate the quantity of strength limiting flaws. Exceptions are found in the “FT float” series, as described above, and the “Schott DURAN tubes” specimens. These borosilicate glass samples are in fact formed at a high viscosity ($\approx 10^{4.5}$ dPa s $< T_L$) and are characterized by an increased amount of bubbles (mainly concentrated at the interfaces created between each cullet piece during forming). These bubbles form clusters for crystal growth and if located at the glass surface or at close proximity, they become the strength limiting flaw that leads to fracture (Fig. 39). The flexural data obtained for these two glasses from the 1st series of four-point bending experiments match with the results of the second test.

(b) Contaminated vs. non-contaminated glass specimens

This category studies glass specimens kiln-cast from contaminated cullet, and compares them to the purer

specimens described above. All of the studied specimens, “Float combo”, “Oven doors”, “Car windshields”, and “AGC enamel black” are typical soda lime silicates and have a large amount of distinct crystalline inclusions, and/or heavy cord. Their flexural strength is slightly lower than the one observed for the FT Float specimens and their Young’s moduli are comparable. The “AGC enamel black” series seems to have the highest flexural strength in this category, which is attributed to the fact that only one type of glass is used for the casting of these samples (thus no cord is observed due to minor compositional variations). In addition, the substantial size of the glass pieces allows their thorough cleaning, which is not the case in the smaller sized cullet of the “Oven door” and “Car windshield” samples. All specimens fail at lower values than most of the purer glasses studied above, mainly due to crystalline formations at the surface (Fig. 40). These stones are created either from inherent contamination, or from further reaction of the contaminants with the mould material. The multiple defects located in the bulk of these specimens are not activated during the 4-point bending nor do they seem to reduce the Young’s modulus. On the contrary these defects are tolerated within the glass network. However, the more the defects in the bulk, the more the chances of such flaws to be exposed

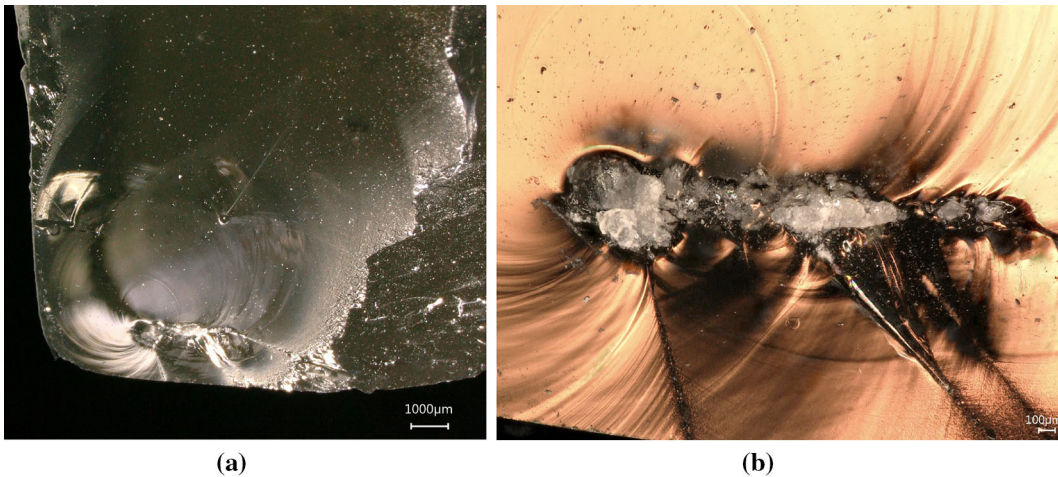


Fig. 39 Microscope images of the fracture origin of a “Schott DURAN tubes 1120 °C” specimen. **a** Incomplete fracture mirror around the origin flaw, which is a crystalline inclusion at 1 mm inside from the bottom surface. This is the only specimen that did

not break at a flaw exactly at the surface. **b** Magnification of the crystalline inclusion, which is clustered together with air bubbles. Early mist and hackle appear within the mirror as a result of interaction of the elastic wave with the defect

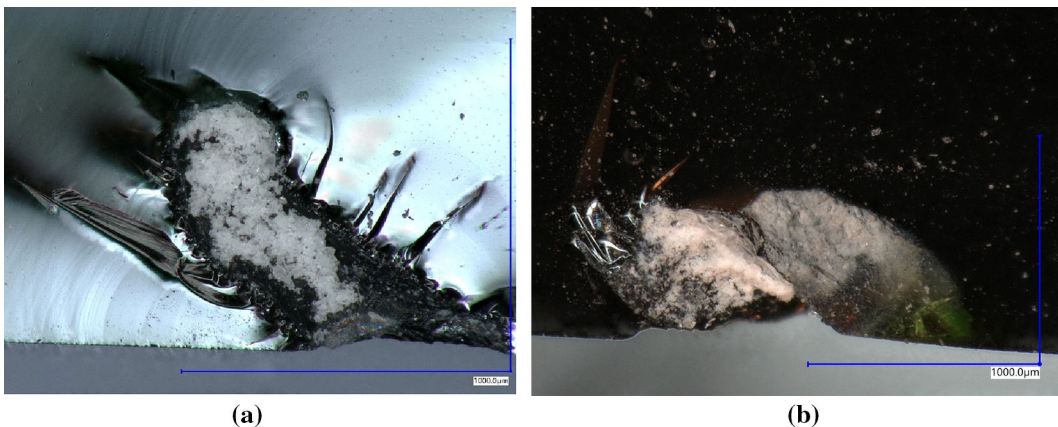


Fig. 40 Microscope images of crystalline formations that function as the origin of fracture in contaminated kiln-cast specimens. The reaction of cullet contaminants (e.g. coatings) with the mould

seem to promote such formations. **a** The stone in the “AGC Float with black enamel, 1120 °C” specimen is adjacent to the enamel interface. **b** Stone in a “Oven doors 1120 °C” specimen

at the surface, and consequently the higher the risk of failure.

(c) Non-contaminated homogeneous glass specimens vs. with crystallized interfaces

In this category, the soda lime and borosilicate glass samples that are kiln-formed at 970 °C and contain structured crystallized interfaces (“Float 1cm, 3 horizontal layers”, “Float 1cm, 24 vertical layers”, “Schott DURAN 10 vertical layers”), are studied in comparison to their more homogeneous versions, kiln-formed at

1070 °C and/or 1120 °C (“FT Float 1120 °C”, “Schott DURAN 10 vertical layers 1070 °C, 1120 °C”). The particular aspect with this category is that the “defects” or zones of compositional/structural variation, are deliberately engineered at specified locations and geometrical patterns. Thus, in antithesis with the random occurrence of stones described in the category above, in this section, the size and distribution of the crystalline formations can be anticipated. As a consequence, their effect on the structural performance can be directly correlated.

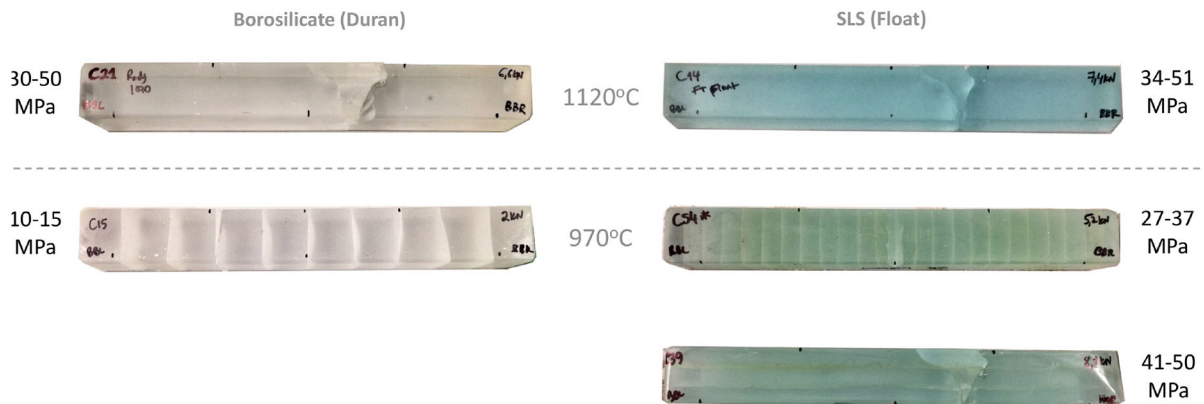


Fig. 41 Fracture pattern and flexural strength range (MPa) of homogeneous (top) and with crystallized interfaces (bottom) specimens. Note that if the crystallized interface is situated only in the bulk (bottom right), the bending strength of the specimen is similar to a homogeneous one (top right). When the crystal-

lized interface is exposed at the bottom surface, the specimens fail at a lower force, from a flaw originating at the glass-crystal interface. Especially in the case of the borosilicate crystallized specimens, the low elastic energy stored results in a single crack without forking

Therefore, it can be observed that the fused “Float 1cm, 3 horizontal layers” specimens present very similar flexural strength and Young’s modulus with the more homogeneous “FT Float” specimens (Fig. 41). This is because the crystalline interfaces are located in the bulk, in parallel layers to the bottom surface, and thus are not exposed to the maximum tensile stress zone. They behave therefore in a similar manner to the homogeneous specimens. This is not the case however with the “Float 1cm, 24 vertical layers” specimens, where the crystalline interfaces are exposed at the bottom surface, and in fact aligned perpendicularly to the tensile forces. Although the Young’s modulus remains similar, the flexural strength is reduced by more than 20%. The fracture origin of these samples is always located at these crystal-glass interfaces and initiates from the glass zone in immediate proximity. The crystalline formations thus seem to act as stress inducing elements, of perhaps higher fracture toughness than the surrounding glass matrix, which weaken the glass specimen.

The type and thickness of the crystalline interface also plays a significant role. The thin b-cristobalite layer created in “Schott DURAN 10 vertical layers 970 °C” results in a dramatic drop of 75% of the strength, and a decrease of the Young’s modulus. The fracture origin is, in a similar manner to the float examples, always located at the crystalline-glass interface.

At this point, knowing the effect of these crystalline formations and their geometrical arrangement, atten-

tion should be raised to the intermediate states between a fused glass specimen produced at viscosities around 10^6 dPa s and a homogeneous specimen cast at temperatures well above the liquidus point (where the rate of diffusion is much higher). Specimens produced at a 10^5 or even a 10^4 dPa s viscosity seem to retain traces of the interface created between each cullet piece during heating up, in the form of subtle bubble veils, cord and spots of crystalline formation. This is evident for example in the “Schott DURAN 10 vertical layers 1070 °C”, kiln-cast at a 10^5 dPa s viscosity (Fig. 42). These samples contained the above described bubble veils and stones in the same geometrical arrangement as the “Schott DURAN 10 vertical layers 970 °C”. These specimens, although stronger than the fused version, had a 30% lower flexural strength than the specimens kiln-cast at a 50 °C higher temperature. They all failed from either a crystalline flaw or a bubble located in one of these veils (Fig. 43). This is a very crucial issue, given the fact that both the 1070 °C and 1120 °C produced specimens look the same and are transparent and not comparable to the contaminated samples described in the category above. This highlights how critical a 50 °C temperature difference can be when casting at viscosities just around and below the liquidus point.

(d) Reference specimens

The industrially manufactured glass specimens are tested in order to provide a point of reference and com-

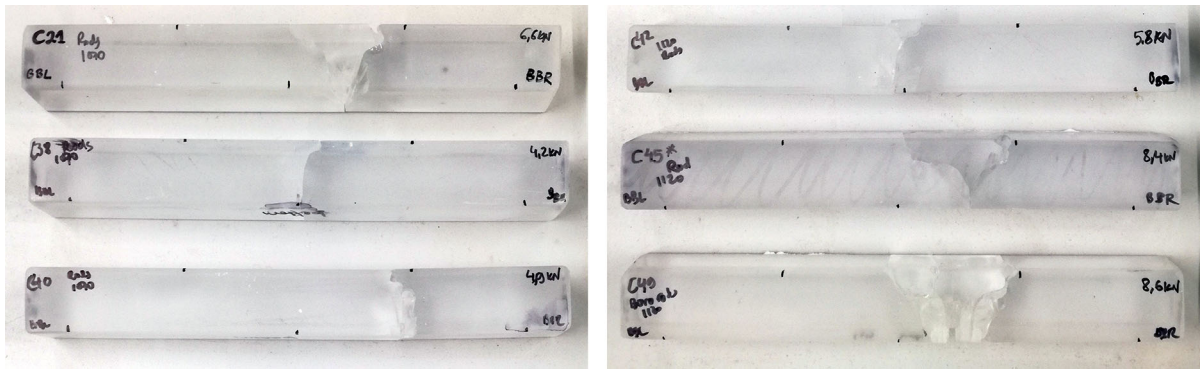


Fig. 42 “Schott DURAN 10 vertical layers” specimens produced at 1070 °C (left column) and 1120 °C (right column). The remnant bubble veils in the specimens produced at a lower tem-

perature result in a lower flexural strength. The origin of fracture in these specimens can be found in one of these bubble veils

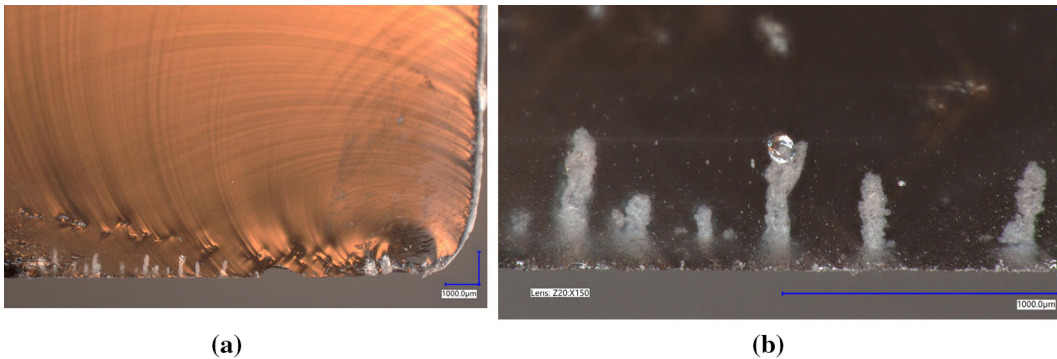


Fig. 43 Microscope images of the fracture mirror of a “Schott DURAN 10 vertical layers, 1070 °C” specimen. **a** Succession of air bubbles close to the bottom surface, interacting with the elastic wave. The cause of fracture is a stone formation (right end of the picture) in proximity to the bubble clustering. **b** Magnification of stone formations extending from the surface to the bulk.

Their perpendicular to the surface direction and the presence of a bubble, suggest that these stones are formed from the interaction of the mould material with the bubbles created at the fusion interface between the glass rods during forming at a favourable for crystallization-temperature

parison with the kiln-cast glass samples. Their structural performance is described below per type.

The beams cut out from standard Poesia cast glass bricks (originally hot poured at around 1200 °C) are more homogeneous than the kiln-cast specimens produced in the lab. Apart from some minor striae and few bubbles, they do not contain critical defects such as stones, since the purity of the raw source, the above liquidus point forming temperature, the abrupt quenching at atmospheric conditions, and the stainless steel moulds used for their casting, prevent their formation. Nonetheless, these specimens present a 10% lower flexural strength than the less homogeneous, re-cast specimens at 1070 °C. This is attributed to the

faster annealing scheme followed for these components, which causes residual stresses frozen in the glass, and makes it more susceptible to damage. As a consequence, during the cutting and grinding of the component in size, multiple chips and resulting cleavage damage are caused due to insufficient annealing, which are not entirely removed during polishing. The added stress and machining defects are the cause of fracture, at a lower strength.

Considering the single float glass pane specimens, these are the most homogeneous of all studied samples, with a pristine polished bottom and top surface. Since these specimens are cut out from larger float panels, their edges are ground and polished as described in

Sect. 2.1. All single pane samples from the first series of four-point bending experiments failed from a machining flaw at the edge, within the bottom zone of maximum tensile stress. The average flexural strength for the 10 mm panes is 55 MPa, which is 20% higher than the “FT Float 1120 °C” specimens but 20% lower than the highest scoring specimens “AGC dark blue 1120 °C” and the “Poesia 1070 °C”. Undoubtedly, the quality of the bottom edges can dramatically affect the flexural strength of the float glass sample in bending. According to the size and the polishing quality of the samples, and the test settings, a wide range of flexural strengths in 4 point-bending are reported in literature, from 35 to 170 MPa (Veer and Rodichev 2011), 51–71.5 MPa (Veer 2007), 53–129 MPa (Yankelevsky et al. 2016) to name a few. The 55 MPa strength of the tested samples in this study is at the low end of this range, and in line with the literature, given the relatively rough edge finishes. A much higher strength could be expected with finer polishing. In that sense and taking into account that the kiln-cast specimens exhibiting higher tensile strengths failed as well from machining flaws, it can be derived that a much higher strength is possible with the industrial fine polishing of the kiln-cast specimens.

The beams produced from adhesively bonded (Delo Photobond 4468) 8/10 mm thick float glass plies, and tested with their plies parallel to the bottom surface, have an average flexural strength of 48 MPa (1st and 2nd four point bending series), which is 10% higher than the kiln-formed “FT Float 1120 °C” specimens. None of the specimens failed from an edge flaw; the cause of failure is attributed to minor handling damage at the bottom surface. The Young’s modulus of the adhesively bonded beams is lower than that of the monolithic, kiln-cast SLS specimens, due to the adhesive layers.

Overall, the flexural strength values obtained from the industrially produced reference samples are at the top end of the 30–55 MPa (second) zone, and do not exceed the performance of the purest kiln-cast samples (found in the first zone). This is an encouraging result, given the fact that all the kiln-cast specimens produced for this study have some level of inhomogeneities.

5 Conclusions

A variety of commercial glass waste types is tested for the ability to be kiln-cast into structural components

at relatively low temperatures (820–1120 °C), and the flexural strength of the kiln-cast specimens is evaluated.

The kiln-casting experiments show that meticulous separation of cullet at the recycling facilities guarantees a successful casting. Coatings and traces of external contaminants such as organics and metals are tolerated by the glass network yet lead to defects and low flexural strength, while contamination by glass ceramics and glasses with significant compositional variations causes the fracture of the specimens during cooling. Glass compositions with a lower liquidus point facilitate low temperature kiln-casting which leads to more homogeneous glass surfaces, as the lower viscosity during forming minimizes the occurrence of sintering flaws, surface bubbles and stone formation from mould contamination.

Regarding the four-point bending experiments, although the number of tested specimens per glass type is not sufficient for deriving statistical data, they do provide a good overview and reasonable estimate of the structural performance of each specimen type, according to the chemical composition, level of contamination, and followed casting parameters.

The effect of the chemical composition on the strength is distinctly observed in the specimens produced from purer cullet and at higher forming temperatures. Among these samples, a clear increase in the strength and Young’s modulus is observed, consecutively from the lead silicate, to the borosilicate, barium silicate and up to the soda lime silicate family. The purer, more homogeneous samples predominantly fail from external defects induced by machining and handling damage. The effect of the composition is however blurred in the more contaminated samples, where crystalline formations formed at the bottom surface within the zone of maximum tensile stress, are the prevailing cause of fracture leading to a significantly lower strength.

Within the soda lime silica family, particularly promising are the slightly modified recipes containing small amounts of K_2O and B_2O_3 and a higher Na_2O to CaO ratio. The lower viscosity of these glass melts facilitates the casting process, while their more open structure (higher molar volume) presents a less brittle alternative for a similar Young’s modulus to that of SLS glasses, leading eventually to a higher flexural strength.

Glass families of an even lower liquidus point, such as the studied lead silicate and barium silicate samples, are attractive for lower energy manufactur-

ing. However, for structural applications demanding higher strength, the barium silicate option is much more promising due to the higher E modulus and less susceptibility to scratching.²⁶

Regarding the more inhomogeneous specimens, produced from contaminated cullet at temperatures around the liquidus point, they still present a good flexural strength and are suitable for structural applications demanding lower tensile strength, such as bricks. The flaws occurring in the bulk are not activated during the four-point bending test and have a minor or even negligible contribution to the strength and E modulus. However, an increased density of defects in the bulk should imply a higher density of flaws at the surface as well, which should lead to an average strength reduction. A higher forming temperature (above the liquidus point) would significantly help in diminishing the amount of flaws, but considering the economic and environmental advantages of lower temperature processing, such an act would be only meaningful if higher design strengths were required per specific case.

Crystallized geometrical structures are induced within soda-lime-silica and borosilicate specimens produced at higher viscosities (10^6 – 10^5 dPa s). If these structures are located in the bulk, the flexural strength of the specimen is equal to that of a more homogeneous casting at a higher temperature (close to the liquidus point). However, the exposure of such structures at the surface subjected in tension can lead to a dramatic decrease of strength of even 75% according to the nature of the produced crystalline formations. In this case, the origin of fracture always occurs in the glass/crystal interface. Specific attention should be given to castings formed at between 10^5 – 10^4 dPa s viscosities, as the glass products may appear homogeneous but retain significant inhomogeneous zones of miniscule bubbles and stones at the former interface created between each cullet pieces during heating up. Such formations exposed at the tensile surface are critical for the specimen's strength.

Industrially SLS manufactured glass samples, post-processed in the lab facilities to match the studied specimen size, present similar flexural strength to that of the

float glass kiln-cast specimens (at 1120 °C), yet score at the lower end of strength values reported in the literature. Machining flaws from the processing to size, and insufficient annealing in the case of the cast bricks, are the factors responsible for the lower strength. A finer polishing would significantly increase the strength, not only of these samples, but also of the purer kiln-cast specimens. However, given that the lowest strength specimens would be less affected by a finer polishing quality, the statistical strength would not be increased that much, as it is dominated by these lower outliers.

6 Recommendations

The results of this study show the potential of recycling waste glass into cast structural building components. However, for the safe application of such products, further validation is required and an increased number of tested specimens per category (≥ 30 , Quinn et al. 2009) is needed to derive statistical predictions. In particular, the repetition of testing is of crucial importance in the case of the contaminated samples, where a higher degree of variability is expected in the mechanical properties. The systematic testing of such samples should be linked with a quantified documentation of the type and level of inhomogeneities in the glass prior to testing. Careful and extensive fracture analysis of the tested specimens is also necessary to identify the most critical defects, and the relationship of the flaw size to the flexural strength. The physiochemical identification of the crystalline formations at the glass surface by scanning electron microscopy is required for categorizing such critical flaws. Further testing is necessary, as well, to determine the influence of scale factor, and of static fatigue in moist environments (effect of slow crack growth). In addition, the studying of the behaviour of crystalline inclusions in the bulk glass under thermal gradients relevant to building applications is important to eliminate the risk of thermal cracking. Additional, non-destructive testing for determining the Young's modulus and the level of inhomogeneities in the cast glass is also suggested, implementing the Impulse Excitation Technique. Investigation of whether such a fast and inexpensive non-destructive technique could serve as a quality control method for cast glass products is worth exploring.

Regarding the more contaminated components, attention should be given in improving the quality of the

²⁶ Yamane and Mackenzie (1974) prove in their model the proportional relationship of Vicker's hardness to the Young's modulus and bond strength. As a point of reference, Ainsworth's (1954) measurement of Vicker's hardness for a $18\text{Na}_2\text{O} \cdot 10\text{BaO} \cdot 72\text{SiO}_2$ (mol%) glass is 522 kg/mm² and for a $18\text{Na}_2\text{O} \cdot 10\text{PbO} \cdot 72\text{SiO}_2$ (mol%) glass 445 kg/mm².

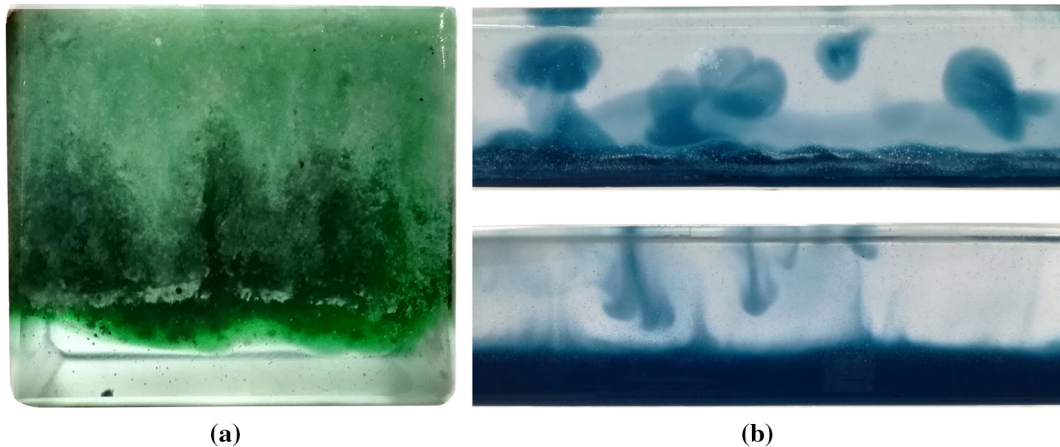


Fig. 44 Prototypes of composite kiln-cast glass components, containing a purer glass at the bottom and a weaker, more contaminated glass at the bulk and top zone. **a** Gradient from a pure transparent soda lime silica glass (bottom) to a partially crys-

tallized zone produced from waste glass powder (residue from the glass container recycling process). **b** Reinforcement of a “FT Float” glass beam by a bottom layer comprising the stronger “ACG blue” glass

stone-containing surface of the recycled glass. Chemical strengthening of the surface by ion exchange could be a—high cost—solution although this is not likely to help with deep defects. Another simpler solution applicable for high viscosity castings (where the diffusion rate is low), is the structuring of two (compatible) cullet qualities inside the mould: a purer along the demanding zones, and a lower more contaminated quality in the bulk (Fig. 44). Such a composite glass would enable the use of contaminated, unwanted cullet without necessarily compromising the strength of the final product.

Lastly, the engineering of crystalline or bubble veil geometrical structures within the glass is worth further exploration, as they can lead to fractures within a predictable strength range and location. They also can lead to building components with non-standard appearance and thus higher architectural appeal.

Acknowledgements The authors would like to express their gratitude to Giorgos Stamoulis for his significant contribution in preparing the four-point bending experiment and DIC measurements, as well as Kees van Beek for his guidance. We are particularly grateful to George Quinn and James Varner for their valuable input regarding the experimental procedure and the fracture analysis of the results. The feedback received from Bert Sluijs, Mauro Overend, Christian Louter and Karl-Heinz Wolf is highly appreciated. We would also like to thank Ruud Hendrikx for the XRF and XRD analyses, Mariska van der Velden for assisting in the specimen preparation, Sander van Asperen and Wolfgang Gard for providing access to their labs’ Keyence digital microscopes, and Henning Katte and Daniel Schreinert (Ilis) for sponsoring the use of StrainScope Flex. The authors are

also very grateful to Cor Wittekoek (Vlaktglasrecycling), Danny Timmers (Maltha Glasrecycling Nederland), Marco Zaccaria and François Boland (AGC Belgium), Brian Wittekoek (Coolrec), Bettina Sommer (Royal Leerdam Crystal), and Klaas Roelfsema (Schott), for the glass cullet contribution, which was of key importance for this work. Finally, we would like to thank Erik Muijsenberg (Glass Service) for the “Glass Defects” (Bartuška 2008) book, and Peter de Haan (AGR Delft) for the “Color Atlas of Container Defects” (Aldinger and de Haan 2019) and “Color Atlas of Stones in Glass” (Aldinger and Collins 2016) books, which were very helpful in the process of defect categorization and identification.

Compliance with ethical standards

Conflict of interest On behalf of all authors, the corresponding author states that there is no conflict of interest.

Open Access This article is licensed under a Creative Commons Attribution 4.0 International License, which permits use, sharing, adaptation, distribution and reproduction in any medium or format, as long as you give appropriate credit to the original author(s) and the source, provide a link to the Creative Commons licence, and indicate if changes were made. The images or other third party material in this article are included in the article’s Creative Commons licence, unless indicated otherwise in a credit line to the material. If material is not included in the article’s Creative Commons licence and your intended use is not permitted by statutory regulation or exceeds the permitted use, you will need to obtain permission directly from the copyright holder. To view a copy of this licence, visit <http://creativecommons.org/licenses/by/4.0/>.

References

- Abrisa Technologies: SCHOTT Duran® Lab Glass (Tubed) (2014)
- Ainsworth, L.: The diamond pyramid hardness of glass in relation to the strength and structure of glass. *Soc. Glass Technol.* **38**, 501–547 (1954)
- Aldinger, B.S., Collins, B.K.: *Color Atlas of Stones in Glass*. American Glass Research, Butler (2016)
- Aldinger, B.S., de Haan, P.W.: *Color Atlas of Glass Container Defects*. American Glass Research, Butler (2019)
- Andreola, F., Barbieri, L., Corradi, A., Lancellotti, I., Falcone, R., Hreglich, S.: Glass-ceramics obtained by the recycling of end of life cathode ray tubes glasses. *Waste Manag.* **25**, 183–189 (2005). <https://doi.org/10.1016/j.wasman.2004.12.007>
- ASM International: *Applications for Glasses Engineered Materials Handbook Desk Edition*. ASM International (1995)
- Bartuška, M.: *Glass Defects*. Glass Service Inc. and Práh, Prague (2008)
- Brennan, J.J.: *Program to Study SiC Fiber Reinforced Glass Matrix Composites*. United Technologies Research Center, Connecticut (1979)
- Bristogianni, T., Oikonomopoulou, F., Justino de Lima, C.L., Veer, F.A., Nijssse, R.: *Structural Cast Glass Components Manufactured from Waste Glass: Diverting Everyday Discarded Glass from the Landfill to the Building Industry*. Heron 63 (1/2 Special issue: Structural Glass) (2018)
- Bristogianni, T., Oikonomopoulou, F., Veer, F.A., Nijssse, R.: The effect of manufacturing flaws in the meso-structure of cast glass on the structural performance. In: Zingoni, A. (ed.) *Advances in Engineering Materials, Structures and Systems: Innovations, Mechanics and Applications*, pp. 1703–1708. CRC Press, Leiden (2019)
- Burch, O.G., Babcock, C.L.: Effect of glass color on setting rates in manufacture of glass bottles. *J. Am. Ceram. Soc.* **21**(10), 345–351 (1938)
- Campbell, D.E., Hagy, H. E.: *Glasses and Glass-Ceramics*. In: Lynch, C.T. (Ed.) *CRC Handbook of Materials Science*, vol. II: *Material Composites and Refractory Materials*. CRC Press, USA (1975)
- Chyung, K.: *Transparent Beta-Quartz Glass Ceramics*. Corning Glass Works, United States Patent US4018612A (1977)
- Corning: *Properties of Corning's Glass and Glass Ceramic Families*. In: *Materials for the Design Engineer*. USA (1979)
- Fluegel, A.: Glass viscosity calculation based on a global statistical modeling approach. *Glass Technol. Eur. J. Glass Sci. Technol. A* **48**, 13–30 (2007a)
- Fluegel, A.: Global model for calculating room-temperature glass density from the composition. *J. Am. Ceram. Soc.* **90**, 2622–2625 (2007b). <https://doi.org/10.1111/j.1551-2916.2007.01751.x>
- Friedrich & Dimmock Inc.: *Comparative Values of Borosilicate Glasses*. In: *Simax Glass Properties*
- Gold Star: *Investment Casting Powder Safety Data Sheet*, www.goldstarpowders.com (2019)
- Goodwin Refractory Services Ltd: *Crystalcast (M248)*. www.grscastingpowders.com (2003)
- Gregory, C.: *Hollow Fibers*. In: Sanghera, J.S.A., I.D. (ed.) *Infrared Fiber Optics*. CRC Press LLC, USA (1998)
- Heimerl, W.: *Chemical resistance and corrosion, and ion release*. In: Bach, H., Krause, D. (eds.) *Analysis of the Composition and Structure of Glass and Glass Ceramics*. Springer, Berlin (1999)
- Höland, W., Beall, G.H.: *Glass—Ceramic Technology*, 3rd edn. Wiley, Hoboken (2020)
- Inaba, S., Fujino, S., Morinaga, K.: Young's modulus and compositional parameters of oxide glasses. *J. Am. Ceram. Soc.* **82**, 3501–3507 (1999). <https://doi.org/10.1111/j.1151-2916.1999.tb02272.x>
- Ito, S., Taniguchi, T.: Effect of cooling rate on structure and mechanical behavior of glass by MD simulation. *J. Non-Cryst. Solids* **349**, 173–179 (2004). <https://doi.org/10.1016/j.jnoncrysol.2004.08.180>
- Kitaigorodskii, I.I., Solomin, N.W.: Rate of setting of glass during working. *Soc. Glass Technol.* **18**, 323–335 (1934)
- Makishima, A., Mackenzie, J.D.: Direct calculation of Young's modulus of glass. *J. Non-Cryst. Solids* **12**(1), 35–45 (1973). [https://doi.org/10.1016/0022-3093\(73\)90053-7](https://doi.org/10.1016/0022-3093(73)90053-7)
- Martienssen, W., Warlimont, H.: *Springer Handbook of Condensed Matter and Materials Data* (2005)
- MatWeb: *C-Glass Fiber*. www.matweb.com
- Montazerian, M., Singh, S.P., Zanotto, E.: An analysis of glass-ceramic research and commercialization. *Am. Ceram. Soc. Bull.* **94**, 30–35 (2015)
- Morey, G.W.: The effect of boric oxide on the devitrification of the soda-lime-silica glass Na₂O–CaO–B₂O₃–SiO₂. *Quat. Syst.* **15**(9), 457–475 (1932). <https://doi.org/10.1111/j.1151-2916.1932.tb13959.x>
- Mueller, J., Boehm, M., Drummond, C.: Direction of CRT waste glass processing: electronics recycling industry communication. *Waste Manag.* **32**, 1560–1565 (2012). <https://doi.org/10.1016/j.wasman.2012.03.004>
- National Institutes of Health (NIH): *PubChem database*. <https://pubchem.ncbi.nlm.nih.gov/>
- Oikonomopoulou, F., Bristogianni, T., Veer, F.A., Nijssse, R.: The construction of the crystal Houses façade: challenges and innovations. *Glass Struct. Eng.* **3**(1), 87–108 (2018a). <https://doi.org/10.1007/s40940-017-0039-4>
- Oikonomopoulou, F., Bristogianni, T., Barou, L., Jacobs, E., Frigo, G., Veer, F.A., Nijssse, R.: Interlocking cast glass components, exploring a demountable dry-assembly structural glass system. *Heron* **63**, 103–138 (2018b)
- Oikonomopoulou, F., Bristogianni, T., Barou, L., Veer, F.A., Nijssse, R.: The potential of cast glass in structural applications. Lessons learned from large-scale castings and state-of-the-art load-bearing cast glass in architecture. *J. Build. Eng.* **20**, 213–234 (2018c). <https://doi.org/10.1016/j.job.2018.07.014>
- Priven, A.I.: Evaluation of the fraction of fourfold-coordinated boron in oxide glasses from their composition. *Glass Phys. Chem.* **26**(5), 441–454 (2000). <https://doi.org/10.1007/BF02732065>
- Quinn, G.D.: *NIST Recommended Practice Guide: Fractography of Ceramics and Glasses*, 2nd Ed. (2016)
- Quinn, G.D., Swab, J.J.: Fracture toughness of glasses as measured by the SCF and SEPB methods. *J. Eur. Ceram. Soc.* **37**(14), 4243–4257 (2017). <https://doi.org/10.1016/j.jeurceramsoc.2017.05.012>
- Quinn, G.D., Ives, L.K., Jahanmir, S.: On the nature of machining cracks in ground ceramics: part II—comparison to other

- silicon nitrides and damage maps. *Mach. Sci. Technol.* **9**, 211–237 (2005). <https://doi.org/10.1081/MST-200059051>
- Quinn, G.D., Sparenberg, B.T., Koshy, P., Ives, L.K., Jahanmir, S., Arola, D.D.: Flexural strength of ceramic and glass rods. *J. Test. Eval.* **37**, 222–244 (2009). <https://doi.org/10.1520/JTE101649>
- Schott: Tubular Glass Photobioreactors (2015a)
- Schott: NEXTREMA® (2015b)
- Schott: DURAN Technical Data (2017)
- Sehgal, J., Ito, S.: A New Low-Brittleness Glass in the Soda-Lime-Silica Glass Family. *81(9)*, 2485–2488 (1998). <https://doi.org/10.1111/j.1151-2916.1998.tb02649.x>
- Shelby, J.E.: *Introduction to Glass Science and Technology*. The Royal Society of Chemistry, UK (2005)
- Silva, R.V., de Brito, J., Lye, C.Q., Dhir, R.K.: The role of glass waste in the production of ceramic-based products and other applications: a review. *J. Clean. Prod.* **167**, 346–364 (2017). <https://doi.org/10.1016/j.jclepro.2017.08.185>
- Songhan Plastic Technology Co., L.: Schott Nextrema^{textcircled} 724-3, 712-3 Glass Ceramic
- Specialty Glass Products: STARPHIRE Ultra-Clear™ Soda Lime Glass
- Thompson, D.A.: Low liquidus glasses for television tube face-plates. US Patent US4331770A (1980)
- Veer, F.A.: The strength of glass, a nontransparent value. *Heron* **52**, 87–104 (2007)
- Veer, F.A., Rodichev, Y.: The structural strength of glass: hidden damage. *Strength Mater.* **43**, 302–315 (2011). <https://doi.org/10.1007/s11223-011-9298-5>
- Volf, M.B.: *Chemical Approach to Glass*. Elsevier, Amsterdam (1984)
- Yamane, M., Mackenzie, J.D.: Vicker's Hardness of glass. *J. Non-Cryst. Solids* **15(2)**, 153–164 (1974). [https://doi.org/10.1016/0022-3093\(74\)90044-1](https://doi.org/10.1016/0022-3093(74)90044-1)
- Yankelevsky, D., Spiller, K., Packer, J., Seica, M.: Fracture characteristics of laboratory-tested soda lime glass specimens. *Can. J. Civ. Eng.* (2016). <https://doi.org/10.1139/cjce-2016-0374>
- Yun, Y.H., Bray, P.J.: Nuclear magnetic resonance studies of the glasses in the system Na₂O–B₂O₃–SiO₂. *J. Non-Cryst. Solids* **27(3)**, 363–380 (1978). [https://doi.org/10.1016/0022-3093\(78\)90020-0](https://doi.org/10.1016/0022-3093(78)90020-0)
- Zhdanov, S.P., Shmidel', G.: Coordination state of boron in sodium borosilicate glasses from NMR data. *Fiz. Khim. Stekla* **1(5)**, 452–456 (1975)

Publisher's Note Springer Nature remains neutral with regard to jurisdictional claims in published maps and institutional affiliations.